Banner appropriate to article type will appear here in typeset article

Flow of an Oldroyd-B fluid in a slowly varying contraction: theoretical results for arbitrary values of Deborah number in the ultra-dilute limit

- 4 Evgeniy Boyko¹†, John Hinch² and Howard A. Stone³
- ⁵ Faculty of Mechanical Engineering, Technion Israel Institute of Technology, Haifa 3200003, Israel
- 6 ²DAMTP-CMS, Cambridge University, Wilberforce Road, Cambridge CB3 0WA, UK
- ³Department of Mechanical and Aerospace Engineering, Princeton University, Princeton, NJ 08544, USA
- 8 (Received xx; revised xx; accepted xx)
- Pressure-driven flows of viscoelastic fluids in narrow non-uniform geometries are common 9 in physiological flows and various industrial applications. For such flows, one of the main 10 interests is understanding the relationship between the flow rate q and the pressure drop Δp , 11 which, to date, is studied primarily using numerical simulations. We analyze the flow of 12 the Oldroyd-B fluid in slowly varying arbitrarily shaped, contracting channels and present a 13 theoretical framework for calculating the $q - \Delta p$ relation. We apply lubrication theory and 14 consider the ultra-dilute limit, in which the velocity profile remains parabolic and Newtonian, 15 resulting in a one-way coupling between the velocity and polymer conformation tensor. 16 This one-way coupling enables us to derive closed-form expressions for the conformation 17 tensor and the flow rate-pressure drop relation for arbitrary values of the Deborah number (De). Furthermore, we provide analytical expressions for the conformation tensor and the 19 $q-\Delta p$ relation in the high-Deborah-number limit, complementing our previous low-Deborah-20 number lubrication analysis. We reveal that the pressure drop in the contraction monotonically 21 decreases with De, having linear scaling at high Deborah numbers, and identify the physical 22 mechanisms governing the pressure drop reduction. We further elucidate the spatial relaxation 23 of elastic stresses and pressure gradient in the exit channel following the contraction and show 24 that the downstream distance required for such relaxation scales linearly with De. 25

1. Introduction

26

- Viscoelastic fluid flows in non-uniform geometries consisting of contractions or expansions occur in physiological flows, e.g., arterial flows that may have such shape changes due to thrombus formation (Westein *et al.* 2013), and in various industrial applications (Pearson 1985). For such flows, one of the key interests is to understand the dependence of the pressure drop Δp on the flow rate q. It is well known that adding even small amounts of polymer molecules in a Newtonian solvent may drastically change the hydrodynamic features of the flow of the solution due to polymer stretching, which generates elastic stresses in addition to viscous stresses (Bird *et al.* 1987; Steinberg 2021; Alves *et al.* 2021; Datta *et al.* 2022).
- 35 Pressure-driven flows of viscoelastic fluids and the corresponding flow rate–pressure drop
 - † Email address for correspondence: evgboyko@technion.ac.il

relation have been studied extensively in various geometries, mainly through numerical simulations (Szabo *et al.* 1997; Alves *et al.* 2003; Binding *et al.* 2006; Alves & Poole 2007; Zografos *et al.* 2020; Varchanis *et al.* 2022) and experimental measurements (Rothstein & McKinley 1999, 2001; Sousa *et al.* 2009; Ober *et al.* 2013; James & Roos 2021). We refer the reader to overviews given recently by Boyko & Stone (2022) and Hinch *et al.* (2023).

In particular, the abrupt contraction and contraction—expansion channels have received much attention (Rothstein & McKinley 1999; Alves *et al.* 2003; Binding *et al.* 2006; Ferrás *et al.* 2020), and 4: 1 two-dimensional (2-D) and axisymmetric contraction flows have become benchmark flow problems in computational non-Newtonian fluid mechanics (Alves *et al.* 2021). Numerical simulations of viscoelastic fluid flow in these and other non-uniform geometries include a long downstream (exit) section to allow the stresses to reach their fully relaxed values (see, e.g., Debbaut *et al.* 1988; Alves *et al.* 2003). This is because once perturbed from their fully relaxed values, the elastic stresses require a long distance for spatial relaxation to enable stable and converged numerical solutions. For higher Deborah (*De*) or Weissenberg (*Wi*) numbers (see definitions in § 2.1), a longer downstream section is required (Keiller 1993).

Therefore, understanding the spatial relaxation of elastic stresses, velocity, and pressure is of both fundamental and practical importance, as that determines the size of the computational domain (Alves *et al.* 2003). However, despite extensive study of viscoelastic channel flows, the spatial relaxation of stresses and pressure in these geometries is not well understood. As a result, the length of the exit channel is currently set somewhat arbitrarily, thus motivating the development of theory. Furthermore, in many applications, it is necessary to determine the total pressure drop over the configuration for a given flow rate, thus requiring us to account for the pressure drop in the entry and exit channels. However, most studies to date focused on the non-uniform region or close vicinity of the abrupt contraction and reported a suitably non-dimensionalized so-called Couette correction (or excess pressure drop), rather than the total non-dimensional pressure drop in the entire configuration (see, e.g., Alves *et al.* 2003; Rothstein & McKinley 1999; Binding *et al.* 2006), presumably due to the arbitrariness of the exit channel length in simulations.

One widely used approach to obtaining theoretical results in different viscoelastic fluid flow problems relies on considering the weakly viscoelastic limit by applying a perturbation expansion in powers of the Deborah or Weissenberg number, which are assumed to be small (see, e.g., Datt et al. 2017, 2018; Datt & Elfring 2019; Gkormpatsis et al. 2020; Housiadas et al. 2021; Dandekar & Ardekani 2021; Su et al. 2022). In particular, there have been many applications of such an expansion in conjunction with lubrication theory in studying thin films and tribology problems (Ro & Homsy 1995; Tichy 1996; Sawyer & Tichy 1998; Zhang et al. 2002; Saprykin et al. 2007; Ahmed & Biancofiore 2021; Gamaniel et al. 2021; Ahmed & Biancofiore 2023). Recently, we have applied lubrication theory and such an expansion in powers of De, developing a reduced-order model for the steady flow of an Oldroyd-B fluid in a slowly varying, arbitrarily shaped 2-D channel (Boyko & Stone 2022). We provided analytical expressions for the velocity and stress fields and the flow rate-pressure drop relation in the non-uniform region up to $O(De^2)$. We further exploited the reciprocal theorem (Boyko & Stone 2021, 2022) to obtain the flow rate-pressure drop relation at the next order, $O(De^3)$. Housiadas & Beris (2023) extended the low-Deborahnumber lubrication analysis of Boyko & Stone (2022) to much higher asymptotic orders and provided analytical expressions for the pressure drop up to $O(De^8)$.

However, the low-Deborah-number analysis cannot accurately capture the behavior at high *De* numbers where there are significant elastic stresses. Another approach to simplifying the governing equations while capturing the underlying physics at non-small Deborah numbers is to consider the ultra-dilute limit (Remmelgas *et al.* 1999; Moore & Shelley 2012; Li *et al.*

2019; Mokhtari et al. 2022), $\tilde{\beta} = \mu_p/\mu_0 \ll 1$, where μ_p is the polymer contribution to the 86 total zero-shear-rate viscosity μ_0 of the polymer solution. Physically, the ultra-dilute limit 87 corresponds to a low concentration of polymer molecules in a Newtonian solvent, such that 88 the viscosity of the polymer solution, μ_0 , is only slightly larger than the solvent viscosity, 89 μ_s (Remmelgas et al. 1999; Mokhtari et al. 2022). Furthermore, the limit $\tilde{\beta} = \mu_p/\mu_0 \ll 1$ 90 is closely related to the diluteness criterion of a constant shear-viscosity viscoelastic Boger 91 92 fluid (Moore & Shelley 2012). In the ultra-dilute limit, the flow field approximated as Newtonian creates elastic stresses that are not coupled back to change the flow. These elastic 93 stresses can then be used to find the correction to the velocity and pressure fields due to 94 fluid viscoelasticity, even at high Deborah numbers. Previous studies used this approach to 95 determine the structure of the stress distribution in the flow around a cylinder (Renardy 2000), 96 97 a sphere (Moore & Shelley 2012), and arrays of cylinders (Mokhtari et al. 2022), as well as in the stagnation (Becherer et al. 2009; Van Gorder et al. 2009) and cross-slot (Remmelgas 98 99 et al. 1999) flows.

In this work, we continue our theoretical studies (Boyko & Stone 2022; Hinch et al. 2023) 100 of the pressure-driven flow of the Oldroyd-B fluid in slowly varying, arbitrarily shaped, 101 102 narrow channels. In contrast to Boyko & Stone (2022), who focused only on the flow through a non-uniform channel in the low-Deborah-number limit, and Hinch et al. (2023), who 103 studied numerically the flow through a contraction, expansion, and constriction for order-one 104 Deborah numbers, and also provided an asymptotic description at high Deborah numbers, 105 the current work examines the ultra-dilute limit and arbitrary values of the Deborah number. 106 Specifically, we analyze the flow of the Oldroyd-B fluid in a contracting geometry and the 107 relaxation of the elastic stresses and pressure in the exit channel. We apply the lubrication 108 approximation and use a one-way coupling between the velocity and polymer stresses to 109 derive semi-analytical expressions for the conformation tensor in the contraction and the exit 110 channel for arbitrary values of the Deborah number in the ultra-dilute limit. These semi-111 112 analytical expressions allow us to calculate the pressure drop and elucidate the relaxation of the elastic stresses and pressure in the exit channel for all De. We provide analytical 113 114 expressions for the conformation tensor and the pressure drop in the high-Deborah-number limit, which are consistent with recent results of Hinch et al. (2023), thus complementing our 115 previous low-Deborah-number lubrication analysis (Boyko & Stone 2022). Furthermore, we 116 analyze the viscoelastic boundary layer near the walls at high Deborah numbers and derive the 117 118 boundary-layer asymptotic solutions. Given the well-known lack of accuracy and convergence difficulties associated with the high-Weissenberg-number problem in numerical simulations 119 (Owens & Phillips 2002; Alves et al. 2021), our analytical and semi-analytical results for the 120 ultra-dilute limit, valid at high Deborah numbers, are of fundamental importance as they may 121 serve to validate simulation predictions or be compared with experimental measurements to 122 123 understand more about the applicability of model constitutive equations.

2. Problem formulation and governing equations

124

We analyze the incompressible steady flow of a viscoelastic fluid in a slowly varying and 125 symmetric two-dimensional contraction of height 2h(z) and length ℓ , where $h(z) \ll \ell$, as 126 illustrated in figure 1. Upstream of the contraction inlet (z = 0) there is an entry channel of 127 height $2h_0$ and length ℓ_0 , and downstream of the contraction outlet $(z = \ell)$ there is an exit 128 channel of height $2h_{\ell}$ and length ℓ_{ℓ} . The fluid flow has velocity u and pressure distribution 129 130 p, which are induced by an imposed flow rate q (per unit depth). Our primary interest is to determine the pressure drop Δp over the contraction region and the spatial relaxation 131 132 of pressure and elastic stresses in the exit channel. For our analysis, we shall employ two different systems of coordinates. The first is Cartesian coordinates (z, y) and (z_{ℓ}, y) , where 133

145

146

147

148

149

150

151

159

160

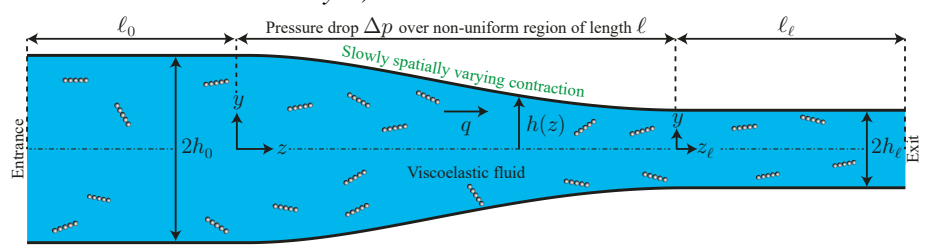


FIGURE 1. Schematic illustration of the two-dimensional configuration consisting of a slowly varying and symmetric contraction of height 2h(z) and length ℓ ($h \ll \ell$). The contraction is connected to two long straight channels of height $2h_0$ and $2h_\ell$, respectively, up- and downstream and contains a viscoelastic fluid steadily driven by the imposed flow rate q.

the z and $z_{\ell} = z - \ell$ axes lie along the symmetry midplane of the channel (dashed-dotted line) and y is in the direction of the shortest dimension. The second one is orthogonal curvilinear coordinates (ξ, η) defined in § 2.3.

We consider low-Reynolds-number flows so that the fluid motion is governed by the continuity equation and Cauchy momentum equations in the absence of inertia

$$\nabla \cdot \boldsymbol{u} = 0, \qquad \nabla \cdot \boldsymbol{\sigma} = \boldsymbol{0}. \tag{2.1a,b}$$

To describe the viscoelastic behavior of the fluid, we use the Oldroyd-B constitutive model (Oldroyd 1950), which represents the most simple combination of viscous and elastic stresses and is used widely to describe the flow of viscoelastic Boger fluids, characterized by a constant shear viscosity. The Oldroyd-B equation can be derived from microscopic principles by modeling polymer molecules as elastic dumbbells, which follow a linear Hooke's law for the restoring force as they are advected and stretched by the flow. The corresponding stress tensor σ is

$$\boldsymbol{\sigma} = -p\mathbf{I} + 2\mu_{s}\mathbf{E} + \boldsymbol{\tau}_{p}, \tag{2.2}$$

where the first term on the right-hand side of (2.2) is the pressure contribution, the second term is the viscous stress contribution of a Newtonian solvent with a constant viscosity μ_s , where $\mathbf{E} = (\nabla \mathbf{u} + (\nabla \mathbf{u})^{\mathrm{T}})/2$ is the rate-of-strain tensor, and the last term, τ_p , is the polymer contribution.

For the Oldroyd-B model, the polymer contribution to the stress tensor τ_p can be expressed in terms of the (symmetric) conformation tensor (or the deformation of the microstructure) **A** as (Bird *et al.* 1987; Larson 1988; Morozov & Spagnolie 2015),

$$\tau_p = G(\mathbf{A} - \mathbf{I}) = \frac{\mu_p}{\lambda} (\mathbf{A} - \mathbf{I}), \tag{2.3}$$

where G is the elastic modulus, λ is the relaxation time, and $\mu_p = G\lambda$ is the polymer contribution to the shear viscosity at zero shear rate. It is also convenient to introduce the total zero-shear-rate viscosity $\mu_0 = \mu_s + \mu_p$.

The evolution equation for the deformation of the microstructure **A** of the Oldroyd-B model fluid is given at steady state as (Bird *et al.* 1987; Larson 1988; Morozov & Spagnolie 2015)

$$\boldsymbol{u} \cdot \nabla \boldsymbol{A} - (\nabla \boldsymbol{u})^{\mathrm{T}} \cdot \boldsymbol{A} - \boldsymbol{A} \cdot (\nabla \boldsymbol{u}) = -\frac{1}{\lambda} (\boldsymbol{A} - \boldsymbol{I}). \tag{2.4}$$

2.1. Scaling analysis and non-dimensionalization

We consider narrow configurations, in which $h(z) \ll \ell$, h_0 is the half-height at z = 0, and $u_c = q/2h_0$ is the characteristic velocity scale set by the cross-sectionally averaged velocity.

We introduce non-dimensional variables based on lubrication theory (Tichy 1996; Zhang *et al.* 2002; Saprykin *et al.* 2007; Ahmed & Biancofiore 2021; Boyko & Stone 2022),

165
$$Z = \frac{z}{\ell}, \qquad Y = \frac{y}{h_0}, \qquad U_z = \frac{u_z}{u_c}, \qquad U_y = \frac{u_y}{\epsilon u_c}, \tag{2.5a}$$

$$P = \frac{p}{\mu_0 u_c \ell / h_0^2}, \qquad \Delta P = \frac{\Delta p}{\mu_0 u_c \ell / h_0^2}, \qquad H = \frac{h}{h_0}, \tag{2.5b}$$

$$\tilde{A}_{zz} = \epsilon^2 A_{zz}, \qquad \tilde{A}_{zy} = \epsilon A_{zy}, \qquad \tilde{A}_{yy} = A_{yy},$$
 (2.5c)

where we have introduced the aspect ratio of the configuration, which is assumed to be small

$$\epsilon = \frac{h_0}{\ell} \ll 1,\tag{2.6}$$

the contraction ratio

$$H_{\ell} = \frac{h_{\ell}}{h_0},\tag{2.7}$$

174 the viscosity ratios

175
$$\tilde{\beta} = \frac{\mu_p}{\mu_s + \mu_p} = \frac{\mu_p}{\mu_0} \quad \text{and} \quad \beta = 1 - \tilde{\beta} = \frac{\mu_s}{\mu_0},$$
 (2.8)

and the Deborah and Weissenberg numbers

$$De = \frac{\lambda u_c}{\ell} \quad \text{and} \quad Wi = \frac{\lambda u_c}{h_0}. \tag{2.9}$$

For lubrication flows through the narrow geometries that we consider, there is a difference between the Deborah and Weissenberg numbers because of the two distinct length scales. The Weissenberg number Wi is the product of the relaxation time scale of the fluid, λ , and the characteristic shear rate of the flow, u_c/h_0 . On the other hand, the Deborah number De is the ratio of the relaxation time, λ , to the residence time in the contraction region, ℓ/u_c , or alternatively, the product of the relaxation time and the characteristic extensional rate of the flow (Tichy 1996; Zhang et al. 2002; Saprykin et al. 2007; Ahmed & Biancofiore 2021). The Deborah and Weissenberg numbers are related through $De = \epsilon Wi$, and for narrow geometries with $\epsilon \ll 1$, De can be small while keeping Wi = O(1).

Similar to our previous study (Boyko & Stone 2022), we non-dimensionalize the pressure using the total zero-shear-rate viscosity $\mu_0 = \mu_s + \mu_p$. However, for convenience, we non-dimensionalize the height based on the entry height rather than the exit height. In addition, unlike our previous study, we do not scale the deformation of the microstructure with De^{-1} . Our current scaling is consistent with a fully developed unidirectional flow of an Oldroyd-B fluid in a straight channel, which yields $\tilde{A}_{zz} = O(De^2)$, $\tilde{A}_{zy} = O(De)$, and $\tilde{A}_{yy} = O(1)$; see (2.10*d*)–(2.10*f*) and (2.16). This scaling is convenient when considering arbitrary and large values of the Deborah number.

Note that, in both Hinch *et al.* (2023) and here, the channel height is 2h, but the total flow rate per unit depth in the former is 2q, whereas in this work it is q as in Boyko & Stone (2022). All results are compatible because the variables used for the non-dimensionalization are the same, i.e., the expressions for the characteristic velocity, characteristic pressure, and the Deborah number are the same.

217

221

228

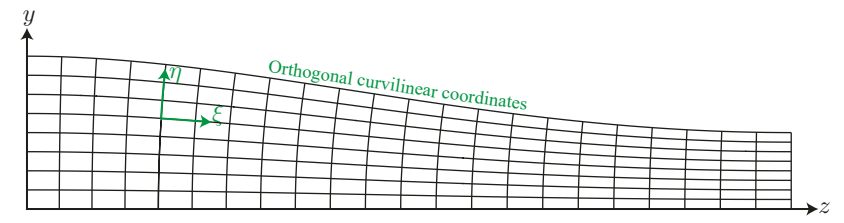


FIGURE 2. Schematic illustration of the orthogonal curvilinear coordinates (ξ, η) for a slowly varying geometry. The coordinate ξ is constant along vertical grid lines, and η , defined in (2.11), is constant along the curves going from left to right.

2.2. Dimensionless lubrication equations in Cartesian coordinates

Using the non-dimensionalization (2.5)–(2.9), to the leading order in ϵ , the governing equations (2.1)–(2.4) take the form

$$\frac{\partial U_z}{\partial Z} + \frac{\partial U_y}{\partial Y} = 0, \tag{2.10a}$$

$$\frac{\partial P}{\partial Z} = (1 - \tilde{\beta}) \frac{\partial^2 U_z}{\partial Y^2} + \frac{\tilde{\beta}}{De} \left(\frac{\partial \tilde{A}_{zz}}{\partial Z} + \frac{\partial \tilde{A}_{zy}}{\partial Y} \right), \tag{2.10b}$$

$$\frac{\partial P}{\partial Y} = 0, \tag{2.10c}$$

$$U_{z}\frac{\partial \tilde{A}_{zz}}{\partial Z} + U_{y}\frac{\partial \tilde{A}_{zz}}{\partial Y} - 2\frac{\partial U_{z}}{\partial Z}\tilde{A}_{zz} - 2\frac{\partial U_{z}}{\partial Y}\tilde{A}_{zy} = -\frac{1}{De}\tilde{A}_{zz}, \qquad (2.10d)$$

$$U_{z} \frac{\partial \tilde{A}_{zy}}{\partial Z} + U_{y} \frac{\partial \tilde{A}_{zy}}{\partial Y} - \frac{\partial U_{y}}{\partial Z} \tilde{A}_{zz} - \frac{\partial U_{z}}{\partial Y} \tilde{A}_{yy} = -\frac{1}{De} \tilde{A}_{zy}, \qquad (2.10e)$$

$$U_{z}\frac{\partial \tilde{A}_{yy}}{\partial Z} + U_{y}\frac{\partial \tilde{A}_{yy}}{\partial Y} - 2\frac{\partial U_{y}}{\partial Z}\tilde{A}_{zy} - 2\frac{\partial U_{y}}{\partial Y}\tilde{A}_{yy} = -\frac{1}{De}(\tilde{A}_{yy} - 1). \tag{2.10}$$

From (2.10*c*), it follows that P = P(Z), i.e., the pressure is independent of Y up to $O(\epsilon^2)$, consistent with the classical lubrication approximation. We note that the scaled \tilde{A}_{zz} on the right-hand side of (2.10*d*) relaxes to ϵ^2 , which is neglected at the leading order in ϵ .

2.3. Orthogonal curvilinear coordinates for a slowly varying geometry

For our theoretical analysis, it is convenient to transform the geometry of the contraction from the Cartesian coordinates (Z, Y) to curvilinear coordinates (ξ, η) , as illustrated in figure 2, with the mapping (Hinch *et al.* 2023)

$$\xi = Z - \frac{1}{2} \epsilon^2 \frac{H'(Z)}{H(Z)} (H(Z)^2 - Y^2) + O(\epsilon^4), \qquad \eta = \frac{Y}{H(Z)}.$$
 (2.11)

As shown in Appendix A, the curvilinear coordinates (ξ, η) are orthogonal with a relative error of $O(\epsilon^4)$, i.e., $\nabla \xi \cdot \nabla \eta = O(\epsilon^4)$.

Hereafter, we use $\mathbf{u} = \mathbf{u}\mathbf{e}_{\xi} + v\mathbf{e}_{\eta}$ and $\mathbf{A} = A_{11}\mathbf{e}_{\xi}\mathbf{e}_{\xi} + A_{12}(\mathbf{e}_{\xi}\mathbf{e}_{\eta} + \mathbf{e}_{\eta}\mathbf{e}_{\xi}) + A_{22}\mathbf{e}_{\eta}\mathbf{e}_{\eta}$ to denote, respectively, the components of velocity and deformation of the microstructure in curvilinear coordinates (ξ, η) . The corresponding non-dimensional velocity components in different coordinates are related through (see Appendix A)

$$U_z = U - \epsilon^2 \eta H'(\xi) V, \qquad U_y = \eta H'(\xi) U + V.$$
 (2.12)

Similarly, the scaled conformation tensor components in different coordinates are related through (see Appendix A)

$$\tilde{A}_{zz} = \tilde{A}_{11} + O(\epsilon^2), \tag{2.13a}$$

$$\tilde{A}_{zy} = \tilde{A}_{12} + \eta H'(\xi) \tilde{A}_{11} + O(\epsilon^2), \tag{2.13b}$$

$$\tilde{A}_{yy} = \tilde{A}_{22} + 2\eta H'(\xi)\tilde{A}_{12} + \eta^2 (H'(\xi))^2 \tilde{A}_{11} + O(\epsilon^2). \tag{2.13c}$$

Finally, we note that, since there is only a $O(\epsilon^2)$ difference between the ξ - and z-directions, for convenience, we continue to use Z rather than ξ in curvilinear coordinates.

2.4. Dimensionless lubrication equations in orthogonal curvilinear coordinates

Using the mapping (2.11), the governing equations (2.10) take the form in curvilinear coordinates (Hinch *et al.* 2023)

$$\frac{\partial(HU)}{\partial Z} + \frac{\partial V}{\partial \eta} = 0, \tag{2.14a}$$

$$\frac{\mathrm{d}P}{\mathrm{d}Z} = (1 - \tilde{\beta}) \frac{1}{H^2} \frac{\partial^2 U}{\partial \eta^2} + \frac{\tilde{\beta}}{De} \left(\frac{1}{H} \frac{\partial (H\tilde{A}_{11})}{\partial Z} + \frac{1}{H} \frac{\partial \tilde{A}_{12}}{\partial \eta} \right),\tag{2.14b}$$

$$U\frac{\partial \tilde{A}_{11}}{\partial Z} + \frac{V}{H}\frac{\partial \tilde{A}_{11}}{\partial \eta} - 2\frac{\partial U}{\partial Z}\tilde{A}_{11} - \frac{2}{H}\frac{\partial U}{\partial \eta}\tilde{A}_{12} = -\frac{1}{De}\tilde{A}_{11}, \qquad (2.14c)$$

$$U\frac{\partial \tilde{A}_{12}}{\partial Z} + \frac{V}{H}\frac{\partial \tilde{A}_{12}}{\partial \eta} - H\frac{\partial}{\partial Z}\left(\frac{V}{H}\right)\tilde{A}_{11} - \frac{1}{H}\frac{\partial U}{\partial \eta}\tilde{A}_{22} = -\frac{1}{De}\tilde{A}_{12},\tag{2.14d}$$

$$U\frac{\partial \tilde{A}_{22}}{\partial Z} + \frac{V}{H}\frac{\partial \tilde{A}_{22}}{\partial \eta} - 2H\frac{\partial}{\partial Z}\left(\frac{V}{H}\right)\tilde{A}_{12} + 2\frac{\partial U}{\partial Z}\tilde{A}_{22} = -\frac{1}{De}(\tilde{A}_{22} - 1). \tag{2.14e}$$

The corresponding boundary conditions on the velocity are

235

238

239

240

247

248

249

252

253

254

255

$$U(Z,1) = 0$$
, $V(Z,1) = 0$, $\frac{\partial U}{\partial \eta}(Z,0) = 0$, $H(Z) \int_0^1 U(Z,\eta) d\eta = 1$, $(2.15a - d)$

which represent, respectively, the no-slip and no-penetration boundary conditions along the channel walls, the symmetry boundary condition at the centerline, and the integral mass conservation along the channel. In addition, we assume a fully developed unidirectional Poiseuille flow in the straight entry channel and the corresponding deformation of the microstructure

$$\tilde{A}_{11} = \frac{18De^2}{H^4}\eta^2, \qquad \tilde{A}_{12} = -\frac{3De}{H^2}\eta, \qquad \tilde{A}_{22} = 1,$$
 (2.16a - c)

with $H \equiv 1$ at the entrance. We also assume that, far downstream in the exit channel, the deformation of the microstructure attains a fully relaxed value, given by (2.16) with $H \equiv H_{\ell}$.

2.5. Pressure drop across the non-uniform region in the lubrication limit

In this subsection, we show that one can calculate the pressure drop without solving directly for the velocity field. To this end, we first integrate by parts the integral constraint (2.15d), repeatedly, using (2.15a) and (2.15c), e.g., (Hinch et al. 2023),

$$256 \qquad \frac{1}{H(Z)} = \int_0^1 U d\eta = \underbrace{\eta U|_0^1}_{0} - \int_0^1 \eta \frac{\partial U}{\partial \eta} d\eta = \underbrace{\frac{1}{2} (1 - \eta^2) \frac{\partial U}{\partial \eta}|_0^1}_{0} - \frac{1}{2} \int_0^1 (1 - \eta^2) \frac{\partial^2 U}{\partial \eta^2} d\eta. \quad (2.17)$$

270

271

272273

274

275

276277

278

279

280

Substituting the expression for $\partial^2 U/\partial \eta^2$ from (2.14b) into (2.17), we obtain

$$-\frac{1-\tilde{\beta}}{H(Z)^3} = \frac{1}{2} \int_0^1 (1-\eta^2) \left[\frac{\mathrm{d}P}{\mathrm{d}Z} - \frac{\tilde{\beta}}{De} \left(\frac{1}{H} \frac{\partial (H\tilde{A}_{11})}{\partial Z} + \frac{1}{H} \frac{\partial \tilde{A}_{12}}{\partial \eta} \right) \right] \mathrm{d}\eta, \tag{2.18}$$

259 which can be rearranged to yield the pressure gradient

$$\frac{dP}{dZ} = -\frac{3(1-\tilde{\beta})}{H(Z)^3} + \frac{3\tilde{\beta}}{2De} \int_0^1 (1-\eta^2) \left[\frac{1}{H(Z)} \frac{\partial (H(Z)\tilde{A}_{11})}{\partial Z} + \frac{1}{H(Z)} \frac{\partial \tilde{A}_{12}}{\partial \eta} \right] d\eta. \quad (2.19)$$

Integrating (2.19) with respect to Z from 0 to 1 provides the pressure drop $\Delta P = P(0) - P(1)$ across the non-uniform region

263
$$\Delta P = 3(1 - \tilde{\beta}) \int_{0}^{1} \frac{dZ}{H(Z)^{3}}$$

$$-\frac{3\tilde{\beta}}{2De} \int_{0}^{1} \int_{0}^{1} (1 - \eta^{2}) \left[\frac{1}{H(Z)} \frac{\partial (H(Z)\tilde{A}_{11})}{\partial Z} + \frac{1}{H(Z)} \frac{\partial \tilde{A}_{12}}{\partial \eta} \right] d\eta dZ. \quad (2.20)$$

Using integration by parts, (2.20) can be expressed as

$$\Delta P = 3(1 - \tilde{\beta}) \int_{0}^{1} \frac{dZ}{H(Z)^{3}} + \frac{3\tilde{\beta}}{2De} \int_{0}^{1} (1 - \eta^{2}) \left[\tilde{A}_{11}(0, \eta) - \tilde{A}_{11}(1, \eta) \right] d\eta$$

$$- \frac{3\tilde{\beta}}{2De} \int_{0}^{1} \left[\frac{H'(Z)}{H(Z)} \left(\int_{0}^{1} (1 - \eta^{2}) \tilde{A}_{11} d\eta \right) \right] dZ - \frac{3\tilde{\beta}}{De} \int_{0}^{1} \left[\frac{1}{H(Z)} \int_{0}^{1} \eta \tilde{A}_{12} d\eta \right] dZ, (2.21)$$

where prime indicates a derivative with respect to Z.

Equation (2.21) resembles the result of an application of the reciprocal theorem previously derived for the pressure drop of the flow of an Oldroyd-B fluid in a slowly varying channel (Boyko & Stone 2021, 2022). The first term on the right-hand side of (2.21) represents the viscous contribution of the Newtonian solvent to the pressure drop. The second term represents the contribution of the elastic normal stress difference at the inlet and outlet of the non-uniform channel. The third term represents the contribution of the elastic normal stresses that arise due to the spatial variations in the channel shape, which is a contribution that is absent in a straight channel. Finally, the last term represents the elastic contribution due to shear stresses within the fluid domain of the non-uniform channel. It should be noted that we do not assume a priori the particular shape of the channel H(Z) but rather consider a flow in a slowly varying channel of arbitrary shape H(Z).

3. Low- $\tilde{\beta}$ lubrication analysis in a slowly varying region

In the previous section, we obtained the dimensionless equations (2.14), which are governed by the two non-dimensional parameters, $\tilde{\beta}$ and De, in the lubrication limit ($\epsilon \ll 1$). In this section, we derive analytical expressions for the velocity, conformation tensor, and the $q - \Delta p$ relation for the pressure-driven flow of a very dilute viscoelastic Oldroyd-B fluid, $\tilde{\beta} = \mu_p/\mu_0 \ll 1$ in a slowly varying channel of arbitrary shape H(Z).

In contrast to our previous study that employed a low-Deborah-number lubrication analysis (Boyko & Stone 2022), in this work, we assume De = O(1) and consider the ultra-dilute limit, $\tilde{\beta} \ll 1$ (see Remmelgas *et al.* 1999; Moore & Shelley 2012; Li *et al.* 2019;

289 Mokhtari et al. 2022). To this end, we seek solutions of the form

$$\begin{pmatrix} U \\ V \\ P \\ \tilde{A}_{11} \\ \tilde{A}_{12} \\ \tilde{A}_{22} \end{pmatrix} = \begin{pmatrix} U_0 \\ V_0 \\ P_0 \\ \tilde{A}_{11,0} \\ \tilde{A}_{12,0} \\ \tilde{A}_{22,0} \end{pmatrix} + \tilde{\beta} \begin{pmatrix} U_1 \\ V_1 \\ P_1 \\ \tilde{A}_{11,1} \\ \tilde{A}_{12,1} \\ \tilde{A}_{22,1} \end{pmatrix} + O(\epsilon^2, \tilde{\beta}^2). \tag{3.1}$$

The ultra-dilute limit represents a one-way coupling between the velocity and pressure fields and the deformation of the microstructure (polymer stresses or conformation tensor). At leading order, the velocity and pressure are Newtonian, and the deformation of the microstructure (i.e., polymer stresses) arises from this Newtonian flow. Accordingly, the velocity and pressure at $O(\tilde{\beta})$ arise due to leading-order polymer stresses. In the next subsections, we provide closed-form asymptotic expressions for the velocity field and conformation tensor components at $O(\tilde{\beta}^0)$ and the pressure drop up to $O(\tilde{\beta})$.

We note that the viscosity ratio $\tilde{\beta} = \mu_p/\mu_0$ is related to the so-called concentration of the polymers $c = \mu_p/\mu_s$ through $\tilde{\beta} = c/(c+1)$. Thus, at the leading order, the limits $\tilde{\beta} \ll 1$ and $c \ll 1$ are identical.

3.1. Velocity, conformation, and pressure drop at the leading order in $\tilde{\beta}$

Substituting (3.1) into (2.14*a*)–(2.14*b*) and considering the leading order in $\tilde{\beta}$, the continuity and momentum equations take the form

$$\frac{\partial (HU_0)}{\partial Z} + \frac{\partial V_0}{\partial \eta} = 0 \quad \text{and} \quad \frac{dP_0}{dZ} = \frac{1}{H^2} \frac{\partial^2 U_0}{\partial \eta^2}, \quad (3.2a, b)$$

subject to the boundary conditions

$$U_0(Z,1) = 0$$
, $V_0(Z,1) = 0$, $\frac{\partial U_0}{\partial \eta}(Z,0) = 0$, $H(Z) \int_0^1 U_0(Z,\eta) d\eta = 1$. $(3.3a - d)$

The solutions for the axial velocity U_0 and the pressure drop ΔP_0 at the leading order are well known (see, e.g., Boyko & Stone 2022)

$$U_0 = \frac{3}{2} \frac{1}{H(Z)} (1 - \eta^2)$$
 and $\Delta P_0 = 3 \int_0^1 \frac{dZ}{H(Z)^3}$. (3.4a, b)

Substituting (3.4a) into the continuity equation (3.2a) and using (3.3b), yields

$$V_0 \equiv 0.$$
 (3.5)

From (3.5), it follows that, in orthogonal curvilinear coordinates, the velocity in the η direction is identically zero at $O(\tilde{\beta}^0)$, in contrast to the Cartesian coordinates where $U_{y,0} = (3/2)H'(Z)Y(H(Z)^2 - Y^2)/H(Z)^4$. As we shall see, this fact significantly simplifies the theoretical analysis and allows us to derive closed-form expressions for the components of the conformation tensor.

Using (3.5), at leading order in $\tilde{\beta}$, the equations for the conformation tensor components, (2.14*c*)–(2.14*e*), simplify to

311
$$U_0 \frac{\partial \tilde{A}_{22,0}}{\partial Z} + 2 \frac{\partial U_0}{\partial Z} \tilde{A}_{22,0} = -\frac{1}{De} (\tilde{A}_{22,0} - 1), \tag{3.6a}$$

313
$$U_0 \frac{\partial \tilde{A}_{12,0}}{\partial Z} - \frac{1}{H} \frac{\partial U_0}{\partial \eta} \tilde{A}_{22,0} = -\frac{1}{De} \tilde{A}_{12,0}, \tag{3.6b}$$

298 299

300

301

290

314
$$U_0 \frac{\partial \tilde{A}_{11,0}}{\partial Z} - 2 \frac{\partial U_0}{\partial Z} \tilde{A}_{11,0} - \frac{2}{H} \frac{\partial U_0}{\partial \eta} \tilde{A}_{12,0} = -\frac{1}{De} \tilde{A}_{11,0}, \tag{3.6c}$$

subject to the boundary conditions

$$\tilde{A}_{11.0}(0,\eta) = 18De^2\eta^2, \qquad \tilde{A}_{12.0}(0,\eta) = -3De\eta, \qquad \tilde{A}_{22.0}(0,\eta) = 1.$$
 (3.7a - c)

- Equations (3.6) represent a set of one-way coupled first-order semi-linear partial differential equations that can be solved first for $\tilde{A}_{22,0}$, followed by $\tilde{A}_{12,0}$, and then for $\tilde{A}_{11,0}$.
- Solving (3.6) together with (3.7), we obtain closed-form expressions for $\tilde{A}_{22,0}$, $\tilde{A}_{12,0}$, and $\tilde{A}_{11,0}$ for arbitrary values of De and the shape function H(Z)

319
$$\frac{\tilde{A}_{22,0}}{H(Z)^2} = e^{f(DeU_0(Z,\eta))} \left[1 + \int_0^Z e^{-f(DeU_0(\tilde{Z},\eta))} \frac{1}{DeU_0(\tilde{Z},\eta)H(\tilde{Z})^2} d\tilde{Z} \right], \quad (3.8)$$
320

$$\frac{\tilde{A}_{12,0}}{(-3De\eta)} = e^{f(DeU_0(Z,\eta))} \left[1 + \int_0^Z e^{-f(DeU_0(\tilde{Z},\eta))} \frac{\tilde{A}_{22,0}(\tilde{Z},\eta)}{DeU_0(\tilde{Z},\eta)H(\tilde{Z})^2} d\tilde{Z} \right], \quad (3.9)$$

$$\frac{\tilde{A}_{11,0}}{18De^2\eta^2/H(Z)^2} = e^{f(DeU_0(Z,\eta))} \left[1 + \int_0^Z e^{-f(DeU_0(\tilde{Z},\eta))} \frac{\tilde{A}_{12,0}(\tilde{Z},\eta)}{(-3\eta De)DeU_0(\tilde{Z},\eta)} d\tilde{Z} \right], \tag{3.10}$$

where $f(DeU_0(Z, \eta))$ is defined as

325
$$f(DeU_0(Z,\eta)) = -\int_0^Z \frac{1}{DeU_0(\tilde{Z},\eta)} d\tilde{Z} = -\int_0^Z \frac{2H(\tilde{Z})}{3De(1-\eta^2)} d\tilde{Z}.$$
 (3.11)

- It is worth noting that the right-hand sides of (3.8)–(3.10) depend on the product $DeU_0(Z, \eta)$
- and are not functions of De and η separately. Furthermore, (3.8)–(3.10) clearly show that,
- while the distribution of $\tilde{A}_{22.0}$ is set solely by the value at the beginning of the non-uniform
- region, the distribution of elastic shear and normal stresses, $\tilde{A}_{12,0}$ and $\tilde{A}_{11,0}$, are coupled to
- the transverse normal stress $\tilde{A}_{22,0}$. In fact, the elastic normal stress $\tilde{A}_{11,0}$ depends both on
- 331 $\tilde{A}_{12,0}$ and $\tilde{A}_{22,0}$.

323

- From (3.8)–(3.10), one might think that the conformation tensor components diverge at
- 333 the wall $(\eta = \pm 1)$. However, using (3.6) and noting that $U_0 = \partial U_0/\partial Z = 0$ at $\eta = \pm 1$, it
- follows that, at the walls of the non-uniform channel,

335
$$\tilde{A}_{22,0}^{\text{wall}} = 1, \qquad \tilde{A}_{12,0}^{\text{wall}} = \mp \frac{3De}{H(Z)^2}, \qquad \tilde{A}_{11,0}^{\text{wall}} = \frac{18De^2}{H(Z)^4} \quad \text{for all } De.$$
 (3.12)

- In §§ 3.1.1 and 3.1.2, we provide explicit expressions for the conformation tensor components
- in the low- and high-De limits. We also note that the results shown in our figure 4(a, c) and
- 338 the work of Hinch et al. (2023) suggest the existence of a viscoelastic boundary layer near
- the walls in the high-De limit, which we analyze in § 3.1.3.
- 3.1.1. Conformation tensor in the low-De limit
- For $De \ll 1$, we solve the equations iteratively for the conformation tensor components (3.6)
- 342 to obtain

343
$$\tilde{A}_{22,0} = 1 + \frac{3DeH'}{H^2} (1 - \eta^2) + \frac{9De^2[4H'^2 - HH'']}{2H^4} (1 - \eta^2)^2 + \frac{27De^3[24H'^3 - 13HH'H'' + H^2H''']}{4H^6} (1 - \eta^2)^3,$$
(3.13a)

346
$$\tilde{A}_{12,0} = -\frac{3De}{H^2}\eta - \frac{18De^2H'}{H^4}\eta(1-\eta^2) - \frac{81De^3[4H'^2 - HH'']}{2H^6}\eta(1-\eta^2)^2, \quad (3.13b)$$

347
$$\tilde{A}_{11,0} = \frac{18De^2}{H^4}\eta^2 + \frac{162De^3H'}{H^6}\eta^2(1-\eta^2) + \frac{486De^4[4H'^2 - HH'']}{H^8}\eta^2(1-\eta^2)^2. \quad (3.13c)$$

- We note that the low-De results (3.13) are consistent with our previous work (Boyko & 348
- Stone 2022), in which we provided explicit expressions for \tilde{A}_{zz} , \tilde{A}_{zy} , and \tilde{A}_{yy} up to $O(De^2)$ 349
- 350
- in Cartesian coordinates. For example, using (2.13c) and (3.13), \tilde{A}_{yy} can be expressed as $\tilde{A}_{yy} = 1 + 3DeH'(Z)(H(Z)^2 3Y^2)/H(Z)^4 + O(De^2)$, in agreement with (3.9a) in Boyko 351
- & Stone (2022). 352
- 3.1.2. Conformation tensor in the high-De limit 353
- We here provide the closed-form expressions for the conformation tensor components in the 354
- high-De limit. We begin with the expression for $\tilde{A}_{22,0}$ and consider the core flow region. 355
- For $De \gg 1$, except close to the wall, (3.6a) reduces to 356

$$U_0 \frac{\partial \tilde{A}_{22,0}}{\partial Z} + 2 \frac{\partial U_0}{\partial Z} \tilde{A}_{22,0} = 0, \tag{3.14}$$

whose solution subject to (3.7c) is 358

359
$$\tilde{A}_{22,0}(Z,\eta) = \tilde{A}_{22,0}(0,\eta) \frac{U_0(0,\eta)^2}{U_0(Z,\eta)^2} = H(Z)^2. \tag{3.15}$$

Next, since $\tilde{A}_{12,0}$ scales as O(De) while $\tilde{A}_{22,0}$ is O(1), within the core flow region in the 360 high-De limit we obtain that the first term in (3.6b) dominates over all the remaining terms 361

$$U_0 \frac{\partial \tilde{A}_{12,0}}{\partial Z} = 0, \tag{3.16}$$

so that elastic shear stresses preserve their value from the entry channel through the non-363 uniform region 364

365
$$\tilde{A}_{12,0}(Z,\eta) = \tilde{A}_{12,0}(0,\eta) = -3De\eta. \tag{3.17}$$

Finally, to determine $\tilde{A}_{11,0}$, we note that the third and fourth terms in (3.6c) scale as O(De), 366

while the first and second terms are $O(De^2)$. Thus, for $De \gg 1$, we expect the first and 367

$$U_0 \frac{\partial \tilde{A}_{11,0}}{\partial Z} - 2 \frac{\partial U_0}{\partial Z} \tilde{A}_{11,0} = 0. \tag{3.18}$$

Solving (3.18) subject to (3.7a) yields 370

371
$$\tilde{A}_{11,0}(Z,\eta) = \tilde{A}_{11,0}(0,\eta) \frac{U_0(Z,\eta)^2}{U_0(0,\eta)^2} = \frac{18De^2\eta^2}{H(Z)^2}.$$
 (3.19)

- In fact, for $De \gg 1$, there is a purely passive response of the microstructure, similar to a 372
- material line element, transported and deformed by the flow without relaxing. 373
- The high-De results (3.15), (3.17), and (3.19) can be also directly obtained from the 374
- closed-form solutions (3.8)–(3.10) by noting that, for $De \gg 1$, $e^{\pm f(DeU_0(Z,\eta))} \approx 1$, and 375
- neglecting the $O(De^{-1})$ terms. 376
- 3.1.3. Boundary-layer analysis in the high-De limit 377
- In the previous section, we obtained analytical expressions for the components of the 378
- conformation tensor in the high-De limit within the core flow region. However, these 379
- expressions do not hold near the walls, where a viscoelastic boundary layer of $O(De^{-1})$ 380
- thickness exists (Hinch et al. 2023). In this section, we analyze this boundary-layer region 381

400

409

382 and provide boundary-layer equations and their closed-form solutions. To this end, we focus on the region $\eta \in [0, 1]$, and introduce the rescaled inner-region coordinate 383

384
$$\zeta = De(1 - \eta) = De\tilde{\eta} \quad \text{for} \quad \tilde{\eta} \ll 1, \tag{3.20}$$

so that $De(1-\eta^2) = \zeta(2-\tilde{\eta}) \approx 2\zeta$. Noting that, in the boundary layer, $\tilde{A}_{22,0} = O(1)$, $\tilde{A}_{12,0} = O(De)$, and $\tilde{A}_{11,0} = O(De^2)$ (see (3.12)), to eliminate the dependence on De in 385

386

the governing equations and boundary conditions (3.7), we rescale $\tilde{A}_{22,0}$, $\tilde{A}_{12,0}$, and $\tilde{A}_{11,0}$, 387

which are functions of Z and ζ , as 388

389
$$\mathcal{A}_{22} = \frac{\tilde{A}_{22,0}}{H(Z)^2}, \qquad \mathcal{A}_{12} = \frac{\tilde{A}_{12,0}}{(-3\eta De)}, \qquad \mathcal{A}_{11} = \frac{\tilde{A}_{11,0}}{18\eta^2 De^2/H(Z)^2}.$$
 (3.21)

Substituting (3.20) and (3.21) into (3.6) and using (3.4a), we obtain the boundary-layer 390 equations in the high-De limit 391

$$\frac{3\zeta}{H(Z)}\frac{\partial\mathcal{A}_{22}}{\partial Z} = -\left(\mathcal{A}_{22} - \frac{1}{H(Z)^2}\right),\tag{3.22a}$$

393 $\frac{3\zeta}{H(Z)}\frac{\partial\mathcal{A}_{12}}{\partial Z}=-(\mathcal{A}_{12}-\mathcal{A}_{22}),$ 394 (3.22b)

 $\frac{3\zeta}{H(Z)}\frac{\partial\mathcal{A}_{11}}{\partial Z} = -(\mathcal{A}_{11} - \mathcal{A}_{12}),$ 396 (3.22c)

subject to the inlet conditions

$$\mathcal{A}_{11}(0,\zeta) = 1,$$
 $\mathcal{A}_{12}(0,\zeta) = 1,$ $\mathcal{A}_{22}(0,\zeta) = 1.$ (3.23*a* – *c*)

Solving (3.22) together with (3.23), we obtain closed-form expressions for \mathcal{A}_{22} , \mathcal{A}_{12} , and 397 \mathcal{A}_{11} in the boundary-layer region 398

399
$$\mathcal{A}_{22} = e^{\mathcal{F}(Z,\zeta)} \left[1 + \int_0^Z e^{-\mathcal{F}(\tilde{Z},\zeta)} \frac{1}{3\zeta H(\tilde{Z})} d\tilde{Z} \right], \tag{3.24a}$$

401
$$\mathcal{A}_{12} = e^{\mathcal{F}(Z,\zeta)} \left[1 + \int_0^Z e^{-\mathcal{F}(\tilde{Z},\zeta)} \frac{\mathcal{A}_{22}(\tilde{Z},\zeta)H(\tilde{Z})}{3\zeta} d\tilde{Z} \right], \tag{3.24b}$$

$$\mathcal{A}_{11} = e^{\mathcal{F}(Z,\zeta)} \left[1 + \int_0^Z e^{-\mathcal{F}(\tilde{Z},\zeta)} \frac{\mathcal{A}_{12}(\tilde{Z},\zeta)H(\tilde{Z})}{3\zeta} d\tilde{Z} \right], \tag{3.24c}$$

where $\mathcal{F}(Z,\zeta)$ is defined as 404

405
$$\mathcal{F}(Z,\zeta) = -\frac{1}{3\zeta} \int_0^Z H(\tilde{Z}) d\tilde{Z}. \tag{3.25}$$

We note that solutions (3.24) satisfy the matching conditions between the inner 406 and outer regions. Specifically, $\mathcal{A}_{22}|_{\zeta\to\infty} = \left[\tilde{A}_{22,0}^{\text{core}}/H(Z)^2\right]_{\eta=1} = 1$, $\mathcal{A}_{12}|_{\zeta\to\infty} = 1$ 407 $\left[\tilde{A}_{12,0}^{\text{core}}/(-3\eta De)\right]_{n=1} = 1$, and $\mathcal{A}_{11}|_{\zeta\to\infty} = \left[\tilde{A}_{11,0}^{\text{core}}/(18\eta^2 De^2/H(Z)^2)\right]_{n=1} = 1$. 408

3.2. Pressure drop at the first order in $\tilde{\beta}$

- Equation (2.20) shows that the pressure drop depends on the elastic normal and shear stresses 410
- \tilde{A}_{11} and \tilde{A}_{12} , and thus, generally, requires the solution of the nonlinear viscoelastic problem. 411
- However, in the ultra-dilute limit, corresponding to $\tilde{\beta} = \mu_p/\mu_0 \ll 1$, we can determine the 412

pressure drop at $O(\tilde{\beta})$ for arbitrary values of De only with the knowledge of the velocity

field and conformation tensor components at O(1). Specifically, substituting (3.1) into (2.20)

415 yields at $O(\tilde{\beta})$ the pressure drop ΔP_1 ,

416
$$\Delta P_{1} = -3 \int_{0}^{1} \frac{dZ}{H(Z)^{3}}$$
417
$$-\frac{3}{2De} \int_{0}^{1} \int_{0}^{1} (1 - \eta^{2}) \left[\frac{1}{H(Z)} \frac{\partial (H(Z)\tilde{A}_{11,0})}{\partial Z} + \frac{1}{H(Z)} \frac{\partial \tilde{A}_{12,0}}{\partial \eta} \right] d\eta dZ, (3.26)$$

418 or alternatively,

419
$$\Delta P_1 = -3 \int_0^1 \frac{dZ}{H(Z)^3} + \frac{3}{2De} \int_0^1 (1 - \eta^2) \left[\tilde{A}_{11,0}(0, \eta) - \tilde{A}_{11,0}(1, \eta) \right] d\eta$$

420 $-\frac{3}{2De} \int_0^1 \left[\frac{H'(Z)}{H(Z)} \left(\int_0^1 (1 - \eta^2) \tilde{A}_{11,0} d\eta \right) \right] dZ - \frac{3}{De} \int_0^1 \left[\frac{1}{H(Z)} \int_0^1 \eta \tilde{A}_{12,0} d\eta \right] dZ.$ (3.27)

Thus, for a given flow rate q, the dimensionless pressure drop $\Delta P = \Delta p/(\mu_0 q \ell/2h_0^3)$, as a

function of the shape function H(Z), the Deborah number De, and the viscosity ratio $\tilde{\beta} \ll 1$,

423 up to $O(\tilde{\beta})$, is given by

$$\Delta P = \Delta P_0(H(Z)) + \tilde{\beta} \Delta P_1(De, H(Z)) + O(\epsilon^2, \tilde{\beta}^2), \tag{3.28}$$

where the expressions for ΔP_0 and ΔP_1 are given in (3.4b) and (3.27), respectively.

Notably, in contrast to our previous results for the pressure drop obtained in the weakly

viscoelastic and lubrication limits with $De \ll 1$ and $\tilde{\beta} \in [0, 1]$ (Boyko & Stone 2022), the

current result (3.28) applies to the limit of $\tilde{\beta} \ll 1$, while allowing De = O(1).

- 429 3.2.1. Pressure drop at $O(\tilde{\beta})$ in the low-De limit
- To calculate the pressure drop ΔP_1 at low Deborah numbers in the non-uniform shape region,
- we use (3.13b)–(3.13c) and (3.27). The elastic normal stress (NS) contribution to the pressure
- 432 drop at $O(\tilde{\beta})$ is

433
$$\Delta P_1^{\text{NS}} = \frac{3}{2De} \int_0^1 (1 - \eta^2) \left[\tilde{A}_{11,0} \right]_{Z=1}^{Z=0} d\eta - \frac{3}{2De} \int_0^1 \left[\frac{H'(Z)}{H(Z)} \left(\int_0^1 (1 - \eta^2) \tilde{A}_{11,0} d\eta \right) \right] dZ$$
434
$$= \frac{27}{10} De(1 - H_\ell^{-4}) \quad \text{for} \quad De \ll 1, \tag{3.29}$$

435 where $\left[\tilde{A}_{11,0}\right]_{Z=1}^{Z=0} = \tilde{A}_{11,0}(0,\eta) - \tilde{A}_{11,0}(1,\eta)$.

The elastic shear stress (SS) contribution to the pressure drop at $O(\tilde{\beta})$ is

437
$$\Delta P_1^{SS} = -\frac{3}{De} \int_0^1 \left[\frac{1}{H(Z)} \int_0^1 \eta \tilde{A}_{12,0} d\eta \right] dZ$$

$$= 3 \int_0^1 \frac{dZ}{H(Z)^3} + \frac{18}{10} De(1 - H_\ell^{-4}) \quad \text{for } De \ll 1. \tag{3.30}$$

Substituting (3.29) and (3.30) into (3.27) provides the pressure drop at $O(\tilde{\beta})$ in the low-*De* limit up to O(De),

$$\Delta P_1 = \frac{9}{2} De(1 - H_{\ell}^{-4}) + O(De^2) \quad \text{for} \quad De \ll 1, \tag{3.31}$$

442 so that the total pressure drop across the non-uniform channel in the low-De limit, accounting

443 for the leading-order effect of viscoelasticity, is

444
$$\Delta P = \underbrace{3(1-\tilde{\beta}) \int_{0}^{1} \frac{dZ}{H(Z)^{3}}}_{\text{Solvent stress}} + \underbrace{3\tilde{\beta} \int_{0}^{1} \frac{dZ}{H(Z)^{3}} + \frac{18}{10} \tilde{\beta} De(1-H_{\ell}^{-4})}_{\text{Elastic shear stress}} + \underbrace{\frac{27}{10} \tilde{\beta} De(1-H_{\ell}^{-4})}_{\text{Elastic normal stress}}$$

$$= 3 \int_{0}^{1} \frac{dZ}{H(Z)^{3}} + \frac{9}{2} \tilde{\beta} De(1-H_{\ell}^{-4}) + O(De^{2}) \quad \text{for} \quad De \ll 1, \quad (3.32)$$

in agreement with the results of our previous work (Boyko & Stone 2022). The three terms on the right-hand side of (3.32) represent, respectively, the Newtonian solvent stress contribution, the elastic shear stress contribution, and the elastic normal stress contribution to the pressure drop.

450 3.2.2. Pressure drop at $O(\tilde{\beta})$ in the high-De limit

To calculate the pressure drop ΔP_1 at high Deborah numbers in the non-uniform region, we use (3.17), (3.19), and (3.27). The elastic normal and shear stress contributions to the pressure drop at $O(\tilde{\beta})$ are

$$\Delta P_1^{\text{NS}} = \frac{9}{5} De(1 - H_{\ell}^{-2})$$
 and $\Delta P_1^{\text{SS}} = 3 \int_0^1 \frac{dZ}{H(Z)}$ for $De \gg 1$. (3.33*a*, *b*)

Substituting (3.33) into (3.27) yields the pressure drop at $O(\tilde{\beta})$ in the high-De limit

$$\Delta P_1 = -3 \int_0^1 \frac{dZ}{H(Z)^3} + 3 \int_0^1 \frac{dZ}{H(Z)} + \frac{9}{5} De(1 - H_\ell^{-2}) \quad \text{for} \quad De \gg 1, \tag{3.34}$$

453 so that the total pressure drop across the non-uniform channel in the high-De limit is

$$\Delta P = \underbrace{3(1-\tilde{\beta})\int_{0}^{1}\frac{dZ}{H(Z)^{3}}}_{\text{Solvent stress}} + \underbrace{3\tilde{\beta}\int_{0}^{1}\frac{dZ}{H(Z)}}_{\text{Elastic shear stress}} + \underbrace{\frac{9}{5}\tilde{\beta}De(1-H_{\ell}^{-2})}_{\text{Elastic normal stress}} \quad \text{for} \quad De \gg 1. \quad (3.35)$$

Similar to the low-De limit, for the contraction geometry, the last term, corresponding to the 455 elastic normal stress contribution, leads to a decrease in the pressure drop, which is linear in 456 the Deborah number. As noted by Hinch et al. (2023), the tension in the streamlines at the end 457 of the contraction pulls the flow through the contraction, thus requiring less pressure to push. 458 Furthermore, at high Deborah numbers, the elastic shear stresses are lower than the fully 459 relaxed value $\tilde{A}_{12} = -3De\eta/H_\ell^2$ due to insufficient time (distance) to approach their fully relaxed value in the contraction. Thus, the elastic shear stress contribution to the pressure 460 461 drop, $3\tilde{\beta} \int_0^1 H(Z)^{-1} dZ$, is smaller than the steady Poiseuille value of $3\tilde{\beta} \int_0^1 H(Z)^{-3} dZ$, further reducing the pressure drop. Finally, we note that the result (3.35) also holds for the 462 463 expansion geometry $H_{\ell} > 1$, in which the two physical mechanisms mentioned above lead 464 to an increase in the pressure drop. 465

4. Low- $\tilde{\beta}$ lubrication analysis in the exit channel

466

In this section, we analyze the spatial relaxation of the elastic stresses and the pressure drop in the uniform exit channel. From examining the expressions (3.8)–(3.10) for the conformation tensor, when there are no longer shape changes, we expect the elastic stresses and the pressure in the exit channel to relax exponentially, with a strong dependence on De^{-1} . Thus, for higher Deborah numbers, a longer downstream section is required (Keiller 1993) for

Contracting channel Exit channel

Deformation of the microstructure:

Described of the interest acture.		
Semi-analytical solution	(3.8)– (3.10)	(B 3)-(B 5)
Low-De asymptotic solution	(3.13)	(B7)
High-De asymptotic solution	(3.15), (3.17), (3.19)	(B9)
Pressure drop:		
Semi-analytical solution	(3.28)	(4.1)
Low-De asymptotic solution	(3.32)	(4.3)
High-De asymptotic solution	(3.35)	(4.4)

Table 1. A summary of the semi-analytical solutions and low- and high-De asymptotic expressions for the deformation of the microstructure and the pressure drop of the Oldroyd-B fluid in a contraction and exit channel in the ultra-dilute limit.

polymer relaxation, consistent with previous numerical simulations using the Oldroyd-B model (Debbaut *et al.* 1988; Alves *et al.* 2003).

Following similar steps as in the previous section, in Appendix B, we derive closed-form expressions for the conformation tensor and the pressure drop in the uniform exit channel for arbitrary values of the Deborah number. Furthermore, we provide analytical expressions for the conformation tensor and the pressure drop in the low- and high-De limits. We summarize in table 1 the semi-analytical solutions and low- and high-De asymptotic expressions for the deformation of the microstructure and the pressure drop of the Oldroyd-B fluid in a contraction and exit channel in the ultra-dilute limit derived in this work.

In particular, we show that the total pressure drop in the exit channel can be expressed as

$$\Delta P_{\ell} = \underbrace{(1 - \tilde{\beta})\frac{3L}{H_{\ell}^{3}}}_{\text{Solvent stress}} + \underbrace{\frac{3\tilde{\beta}}{2De}\int_{0}^{1}(1 - \eta^{2})\left[\tilde{A}_{11,0}\right]_{Z_{\ell}=L}^{Z_{\ell}=0}\mathrm{d}\eta}_{\text{Elastic normal stress}} + \underbrace{\frac{3\tilde{\beta}}{DeH_{\ell}}\int_{0}^{1}\eta\left[\int_{L}^{0}\tilde{A}_{12,0}\mathrm{d}Z_{\ell}\right]\mathrm{d}\eta}_{\text{Elastic shear stress}},$$

$$(4.1)$$

where $L = \ell_\ell/\ell$ is the dimensionless length, $H_\ell = H(Z=1) = h_\ell/h_0$ is the dimensionless height of the exit channel, $Z_\ell = Z - 1$, $\tilde{A}_{11,0}$ and $\tilde{A}_{12,0}$ are given in (B 4) and (B 5), and $\left[\tilde{A}_{11,0}\right]_{Z_\ell=L}^{Z_\ell=0} = \tilde{A}_{11,0}(Z_\ell=0,\eta) - \tilde{A}_{11,0}(Z_\ell=L,\eta)$.

It should be noted that we can express the first-order contribution $\Delta P_{\ell,1}$ in terms of the difference between the conformation tensor components at the beginning and end of the exit channel (see Appendix B and Hinch *et al.* (2023))

489
$$\Delta P_{\ell,1} = \frac{3}{2De} \int_0^1 (1 - \eta^2) \left[\tilde{A}_{11,0} \right]_{Z_{\ell}=L}^{Z_{\ell}=0} d\eta - \frac{9}{2H_{\ell}^2} \int_0^1 \eta (1 - \eta^2) \left[\tilde{A}_{12,0} \right]_{Z_{\ell}=L}^{Z_{\ell}=0} d\eta$$

$$+ \frac{27De}{2H_{\ell}^4} \int_0^1 \eta^2 (1 - \eta^2) \left[\tilde{A}_{22,0} \right]_{Z_{\ell}=L}^{Z_{\ell}=0} d\eta. \tag{4.2}$$

Hereafter, we assume that the length of the exit channel, L, is such that the elastic stresses reach their fully relaxed values by the end of the exit channel, given by (2.16) with $H \equiv H_{\ell}$. Under this assumption, (4.2) clearly shows that the first-order contribution $\Delta P_{\ell,1}$ is *independent* of L since the steady-state values of $\tilde{A}_{11,0}$, $\tilde{A}_{12,0}$, and $\tilde{A}_{22,0}$ depend solely on the η coordinate. Note, however, that the total pressure in the exit channel depends on L via $\Delta P_{\ell} = 3L/H_{\ell}^3 + \tilde{\beta}\Delta P_{\ell,1}$. In addition, we show in Appendix B that the total pressure drop in the exit channel in the

497 low- and high-De limits is

498
$$\Delta P_{\ell} = \frac{3L}{H_{\ell}^{3}} - \frac{1728\tilde{\beta}De^{3}H''(1)}{35H_{\ell}^{7}} \quad \text{for} \quad De \ll 1, \tag{4.3}$$

$$\Delta P_{\ell} = \frac{3L}{H_{\ell}^{3}} + \frac{36}{5}\tilde{\beta}De(H_{\ell}^{-2} - H_{\ell}^{-4}) \quad \text{for} \quad De \gg 1.$$
 (4.4)

From (4.3) and (4.4), it follows that, similar to the contraction, the pressure drop in the exit channel decreases with *De*. Furthermore, the physical mechanisms responsible for the pressure drop reduction are the same in both the contraction and the exit channels.

The asymptotic result (4.4) is obtained using expressions (B 9a)–(B 9c), which hold in the high-De limit within the core flow region. As discussed above, near the walls, there exists a viscoelastic boundary layer of thickness $O(De^{-1})$. Nevertheless, this boundary layer will contribute only a small $O(\tilde{\beta}De^{-1})$ correction to the pressure drop in the exit channel for $De \gg 1$, as noted by Hinch *et al.* (2023).

5. Results

In this section, we present the theoretical results for the pressure drop and conformation tensor distribution of the Oldroyd-B fluid in the ultra-dilute limit developed in §§ 3 and 4. As an illustrative example, we specifically consider the case of a smooth contraction of the form

$$H(Z) = 1 - (1 - H_{\ell})Z^{2}(2 - Z)^{2} \qquad 0 \le Z \le 1,$$
 (5.1)

where $H_{\ell} = H(1)/H(0) = h_{\ell}/h_0$ is the ratio of the exit to entry heights; for the contracting geometry we have $H_{\ell} < 1$. This contraction shape function is illustrated in figure 2 and satisfies H'(0) = H'''(0) = 0 and H'(1) = H'''(1) = 0.

In this work, we present the results for $H_{\ell} = 0.5$ and $\tilde{\beta} = 0.05$. While the current study focuses only on one contraction ratio, in our previous work, we considered four contraction ratios, in which the elastic normal stresses vary by almost two decades (Hinch *et al.* 2023). In addition, figure 8 of our previous paper shows a 0.1 % difference between c = 0.1 and c = 0.05 for the pressure drop in the contraction at De = 0.8. Nevertheless, our current analysis allows us to analyze slowly varying arbitrarily shaped channels provided $\epsilon \ll 1$ and $\tilde{\beta} \ll 1$. To obtain the semi-analytical solutions for given values of De and H_{ℓ} , we first used MATLAB's routine cumtrapz to find the conformation tensor components, given in (3.8)–(3.10) and (B 3)–(B 5), for a contraction and exit channel. Typical values of the grid size were $\Delta Z = 10^{-4}$ and $\Delta \eta = 0.005$. We then used MATLAB's routine trapz to calculate the pressure drop, (3.28) and (4.1), for a contraction and exit channel, respectively.

5.1. Streamwise variation of elastic stresses in the contraction and exit channel

We present in figure 3 the streamwise variation of the leading-order elastic stresses, scaled by their entry values, on $\eta = 0.5$ in contraction and exit channels for De = 0.01 (a, d), De = 0.1 (b, e), and De = 1 (c, f). As expected, for a small Deborah number of De = 0.01, the elastic stresses achieve their downstream fully relaxed values by the end of contraction (figure 3(a)), and thus we observe very little variation in the relaxation along the exit channel (figure 3(d)). Consistent with the low-De asymptotic solutions (3.13), represented by cyan dotted lines, for $H_{\ell} = 0.5$, the elastic shear and axial normal stresses increase by a factor of 4 and 16, respectively, while the transverse normal stress preserves its entry value.

For the case of De = 0.1, shown in figure 3(b, e), the elastic stresses do not have enough residence time to attain their downstream steady-state values in the contraction. Therefore,

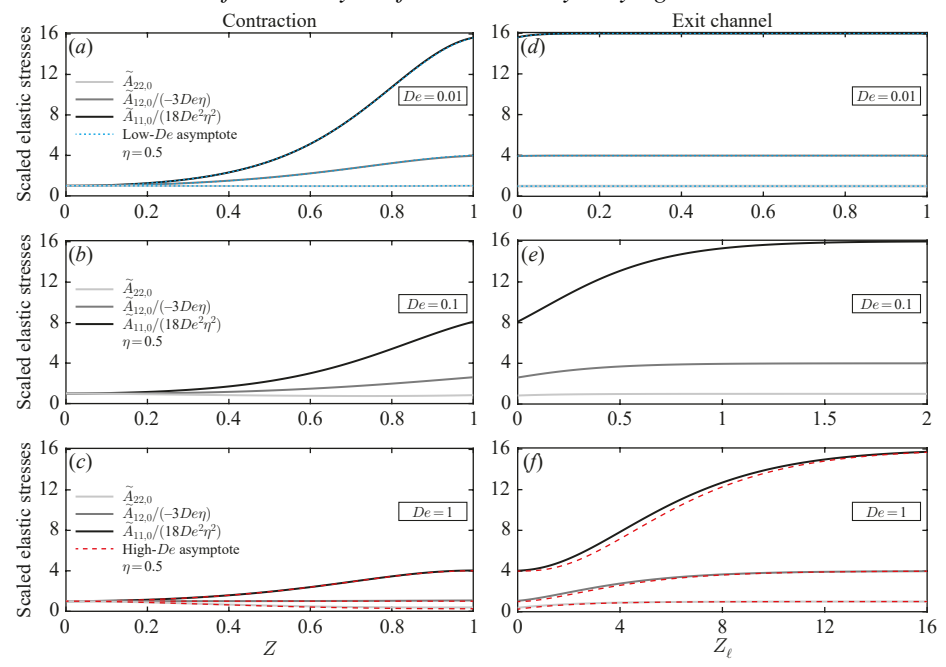


Figure 3. The streamwise variation of leading-order elastic stresses on $\eta=0.5$ in a smooth contraction and exit channel in the ultra-dilute limit. (a-c) Scaled elastic stresses $\tilde{A}_{11,0}/(18De^2\eta^2)$, $\tilde{A}_{12,0}/(-3De\eta)$, and $\tilde{A}_{22,0}$ in the contraction as a function of Z for (a) De=0.01, (b) De=0.1, and (c) De=1. (d-e) Scaled elastic stresses in the exit channel $\tilde{A}_{11,0}/(18De^2\eta^2)$, $\tilde{A}_{12,0}/(-3De\eta)$, and $\tilde{A}_{22,0}$ as a function of Z_ℓ for (d) De=0.01, (e) De=0.1, and (f) De=1. Solid lines represent the semi-analytical solutions (3.8)-(3.10) (contraction) and $(B\ 3)-(B\ 5)$ (exit channel). Cyan dotted lines represent the low-De asymptotic solutions (3.13) (contraction) and $(B\ 7)$ (exit channel). Red dashed lines represent the high-De asymptotic solutions (3.15), (3.17), and (3.19) (contraction) and $(B\ 9)$ (exit channel). All calculations were performed using $H_\ell=0.5$.

there is a significant spatial relaxation in the exit channel. Interestingly, although the relaxation in the exit channel is governed mainly by $e^{-2H_\ell Z_\ell/[3De(1-\eta^2)]}$ (see (B 3)–(B 5)), the elastic stresses relax over slightly different length scales, with the shortest relaxation distance required for $\tilde{A}_{22,0}$ and the longest for $\tilde{A}_{11,0}$. The latter behavior is associated with the nature of the coupling between the elastic stresses so that $\tilde{A}_{11,0}$ depends both on $\tilde{A}_{12,0}$ on $\tilde{A}_{22,0}$, while $\tilde{A}_{12,0}$ depends only on $\tilde{A}_{22,0}$ (see (B 3)–(B 5)).

When De=1, it is evident from figure 3(c) that, at the end of the contraction, the axial normal stress increases by a factor of $1/H_\ell^2=4$, the transverse normal stress is squashed by a factor of $H_\ell^2=1/4$, and the elastic shear stress preserves its entry value. Figure 3(f) presents the spatial relaxation of the elastic stresses in the exit channel for De=1, clearly showing that a very long exit channel is required to attain the downstream fully relaxed values of all stresses (L>16 for $\eta=0.5$). Furthermore, we observe excellent agreement between the semi-analytical results (solid lines) and the high-De asymptotic solutions (3.15), (3.17), (3.19), and (B 9) (dashed red lines). Such an agreement for De=1 is consistent with recent results of Hinch et al. (2023), who found that the high-De analysis works well for De>0.4.

The closed-form solutions for the conformation tensor components, (B 3)–(B 5), clearly show that the spatial relaxation of the elastic stresses in the exit channel strongly depends on the stresses at the end of the contraction (Z = 1). Therefore, it is of particular interest to

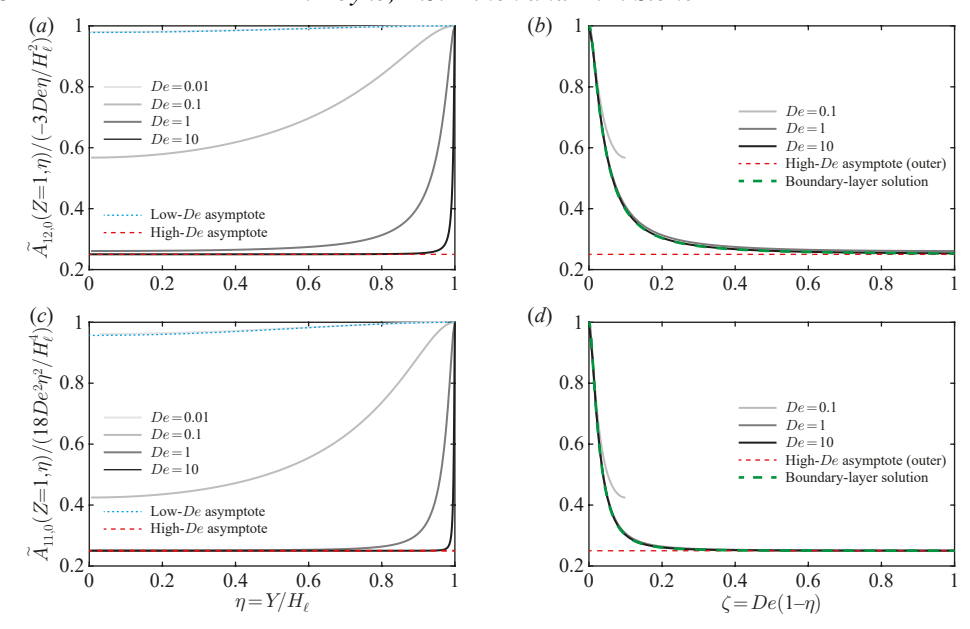
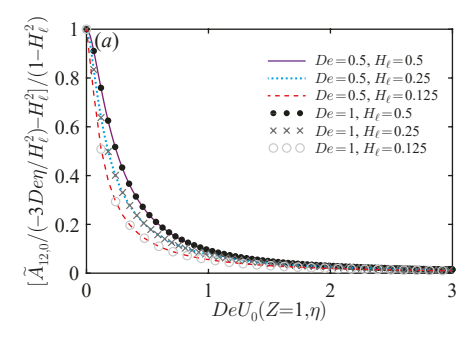


FIGURE 4. The cross-stream variation of leading-order elastic shear and normal stresses at the end of the contraction in the ultra-dilute limit. (a,c) Scaled elastic shear and normal stresses at the end of the contraction, (a) $\tilde{A}_{12,0}(Z=1,\eta)/(-3De\eta/H_\ell^2)$ and (c) $\tilde{A}_{11,0}(Z=1,\eta)/(18De^2\eta^2/H_\ell^4)$, as a function of η for De=0.01,0.1,1, and 10, respectively. (b) $\tilde{A}_{12,0}(Z=1,\eta)/(-3De\eta/H_\ell^2)$ and (d) $\tilde{A}_{11,0}(Z=1,\eta)/(18De^2\eta^2/H_\ell^4)$ as a function of the rescaled coordinate $\zeta=De(1-\eta)$ for De=0.1,1, and 10. Solid lines represent the semi-analytical solutions (3.9)–(3.10). Cyan dotted lines represent the low-De asymptotic solutions (3.13b)–(3.13c). Red dashed lines represent the high-De asymptotic solutions (3.17) and (3.19). Green dashed lines represent the boundary-layer solutions (3.24b)–(3.24c). All calculations were performed using $H_\ell=0.5$.

elucidate the behavior of the elastic stresses at the end of the contraction and the extent to which they are perturbed relative to their downstream fully relaxed values.

The solid lines in figure 4(a,c) present the elastic shear (a) and axial normal stresses (c) at the end of the contraction as a function of $\eta = y/H_{\ell}$ for De = 0.01, 0.1, 1, and 10, scaled by their downstream fully relaxed values. For a small Deborah number of De = 0.01, $\tilde{A}_{12,0}(Z=1,\eta)/(-3De\eta/H_{\ell}^2)$ and $\tilde{A}_{11,0}(Z=1,\eta)/(18De^2\eta^2/H_{\ell}^4)$ only slightly differ from their downstream values, and this behavior is well captured by the low-De asymptotic solutions (3.13b)–(3.13c), represented by cyan dotted lines. As De increases, the elastic stresses become considerably suppressed within the core flow region relative to their eventual relaxed values far downstream, and for De = 1 and De = 10, the elastic shear and axial normal stresses approach the high-De asymptote of $H_{\ell}^2 = 1/4$, represented by red dashed lines. Furthermore, in the high-De limit, we observe the presence of a viscoelastic boundary layer close to the walls, where the elastic stresses reach their downstream fully relaxed values.

To provide insight into this viscoelastic boundary layer, we replot in figure 4(b,d) the elastic shear (b) and axial normal stresses (d) at the end of the contraction as a function of the rescaled coordinate $\zeta = De(1-\eta)$ for De = 0.1, 1, and 10 (see § 3.1.3). It is evident from figures 4(b) and 4(d) that this rescaling collapses the results for the different Deborah numbers onto the same curves, which are the boundary-layer asymptotic solutions (3.24b) and (3.24c) (green dashed lines). Clearly, for De = 1 and De = 10, which are graphically almost indistinguishable, there is excellent agreement between the semi-analytical results



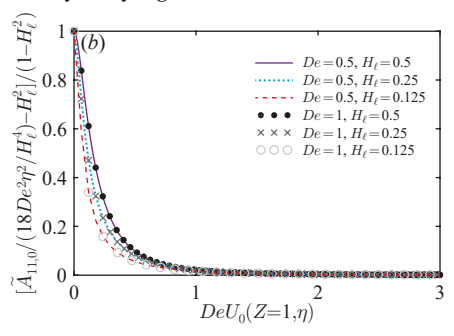


FIGURE 5. (a,b) Scaled elastic shear and normal stresses at the end of the contraction, (a) $\tilde{A}_{12,0}(Z=1,\eta)/(-3De\eta/H_\ell^2)$ and (b) $\tilde{A}_{11,0}(Z=1,\eta)/(18De^2\eta^2/H_\ell^4)$ minus H_ℓ^2 , divided by the factor $1-H_\ell^2$, as a function of $DeU_0(Z=1,\eta)$ for De=0.5,1 and $H_\ell=0.125,0.25$, and 0.5. This rescaling leads to an approximate collapse of the results on the single uniform curve for different Deborah numbers and contraction ratios.

and the boundary-layer asymptotic solutions, thus confirming the thickness of a boundary layer as $O(De^{-1})$.

Furthermore, examining (3.8)–(3.10), we infer that their right-hand sides are not a function of De and η separately but depend on the product $DeU_0(Z,\eta)$. To test this prediction, we show in figure S(a,b) the scaled elastic shear S(a) and axial normal stresses S(a) at the end of the contraction, S(a) and S(a) are S(a) and S(a) and S(a) and S(a) and S(a) and S(a) are contraction of S(a) and S(a) and S(a) are contraction of S(a) and S(a) and S(a) are contraction of S(a) and S(a) are cont

5.2. Pressure gradient relaxation in the exit channel

It follows from figure 3(d-f) in the previous subsection that, as De increases, there is a significant relaxation of the elastic stresses in the exit channel, which occurs over a long distance. Specifically, the elastic stresses relax exponentially over a distance which is proportional to the centerline velocity $(3/2H_{\ell})$ multiplied by the Deborah number De (see (B 3)-(B 5)). For this reason, a longer downstream section is required at higher De.

In this subsection, we study the relaxation of the pressure gradient in the downstream section. Substituting $H(Z) = H_{\ell}$ into (2.19) yields the pressure gradient in the exit channel

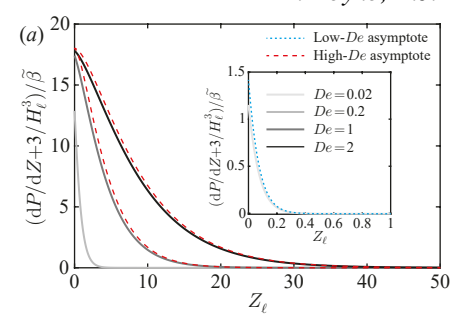
$$\frac{\mathrm{d}P}{\mathrm{d}Z} = -\frac{3(1-\tilde{\beta})}{H_{\ell}^{3}} + \frac{3\tilde{\beta}}{2De} \int_{0}^{1} (1-\eta^{2}) \frac{\partial \tilde{A}_{11,0}}{\partial Z} \mathrm{d}\eta + \frac{3\tilde{\beta}}{H_{\ell}De} \int_{0}^{1} \eta \tilde{A}_{12,0} \mathrm{d}\eta + O(\tilde{\beta}^{2}).$$
 (5.2)

Noting that in the exit channel $U_0 = (3/2H_\ell)(1 - \eta^2)$ and $dU_0/d\eta = -(3/H_\ell)\eta$, and using the expression for $U_0\partial \tilde{A}_{11,0}/\partial Z$ from (B 2c), (5.2) can be written as

$$\left(\frac{\mathrm{d}P}{\mathrm{d}Z} + \frac{3}{H_{\ell}^{3}}\right) \frac{1}{\tilde{\beta}} = \frac{3}{H_{\ell}^{3}} - \frac{H_{\ell}}{De^{2}} \int_{0}^{1} \tilde{A}_{11,0} \mathrm{d}\eta - \frac{3}{H_{\ell}De} \int_{0}^{1} \eta \tilde{A}_{12,0} \mathrm{d}\eta, \tag{5.3}$$

where the right-hand side is independent of $\tilde{\beta}$.

We present in figure 6(a) the relaxation of the scaled pressure gradient $(dP/dZ + 3/H_\ell^3)/\tilde{\beta}$ as a function of the downstream distance Z_ℓ for De = 0.02, 0.2, 1, and 2. Similar to elastic stresses, the scaled pressure gradient relaxes exponentially over the downstream distance, which significantly increases with De. Furthermore, we observe a good agreement between the low- and high-De asymptotic solutions (cyan dotted and red dashed lines) and the semi-analytical results (solid lines).



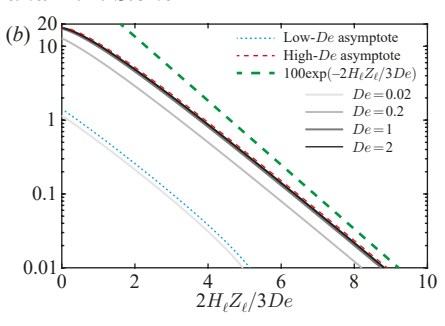


FIGURE 6. The spatial relaxation of the pressure gradient for the Oldroyd-B fluid in the uniform exit channel of a contraction in the ultra-dilute limit. (a) Scaled pressure gradient $(dP/dZ + 3/H_\ell^3)/\tilde{\beta}$ as a function of the downstream distance Z_ℓ for De = 0.02, 0.2, 1, and 2. (b) Scaled pressure gradient $(dP/dZ + 3/H_\ell^3)/\tilde{\beta}$ as a function of the rescaled downstream distance $2H_\ell Z_\ell/3De$ in a log-linear plot. Solid lines represent the semi-analytical solutions obtained from (5.3) using (B 3)–(B 5). Cyan dotted lines represent the low-De asymptotic solutions obtained from (5.3) using (B 7). Red dashed lines represent the high-De asymptotic solutions obtained from (5.3) using (B 9). The green dashed line is $100e^{-2H_\ell Z_\ell/3De}$. All calculations were performed using $H_\ell = 0.5$.

Recalling that the elastic stresses relax exponentially over a distance proportional to $(3De/2H_\ell)$, we replot in figure 6(b) the scaled pressure gradient, (5.3), as a function of the rescaled downstream distance $2H_\ell Z_\ell/3De$ in a log-linear plot. As a result, all curves become parallel to the green dashed line $100e^{-2H_\ell Z_\ell/3De}$, thus confirming that the pressure gradient relaxes over a length scale $\sim (3De/2H_\ell)$, similar to the elastic stresses. More specifically, it follows from figure 6(b) that the downstream distance over which the scaled pressure gradient (PG) decays to 1 % of its maximum value, $L_{1\%}^{PG}$, is approximately

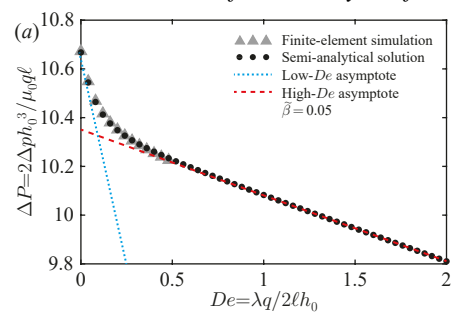
$$L_{1\%}^{PG} \approx (5.3 \pm 0.5) \times \frac{3De}{2H_{\ell}},$$
 (5.4)

where we obtain that the prefactor 5.3 ± 0.5 is weakly dependent on De throughout the investigated range of Deborah numbers. Equation (5.4) and the scaling $3De/2H_{\ell}$ indicate that, in the exit channel, the appropriate Deborah number is based on the exit height, i.e., $De_{\text{exit}} = \lambda q/2h_{\ell}\ell = De/H_{\ell}$.

We note that our estimate of the length of the downstream section, (5.4), is consistent with previous numerical studies on the viscoelastic flows in 2-D abrupt contractions (Debbaut *et al.* 1988; Alves *et al.* 2003). Specifically, (5.4) predicts $L_{1\%}^{PG} \approx 239\pm23$ for $De_{exit} = De/H_{\ell} = 30$, which should be contrasted with 250 of Debbaut *et al.* (1988), who studied numerically the flow through the planar 4:1 contraction.

5.3. Pressure drop in the contraction and exit channel

In this subsection, we study the pressure drop across the contraction and the exit channel. First, in figure 7(a) we present the non-dimensional pressure drop $\Delta P = \Delta p/(\mu_0 q \ell/2h_0^3)$ in the contraction as a function of $De = \lambda q/(2\ell h_0)$ for $H_\ell = 0.5$ and $\tilde{\beta} = 0.05$. For further clarification, figure 7(b) shows the first-order contribution $\Delta P_1 = \Delta p_1/(\mu_0 q \ell/2h_0^3)$ as a function of $De = \lambda q/(2\ell h_0)$, which is independent of $\tilde{\beta}$. Black dots represent the semi-analytical solution (3.28), cyan dotted lines represent the low-De asymptotic solution (3.32), and red dashed lines represent the high-De asymptotic solutions and the semi-analytical results. We also validate the predictions of our semi-analytical and asymptotic results against the 2-D finite-element simulations with $H_\ell = 0.5$, $\tilde{\beta} = 0.05$, and $\epsilon = 0.02$



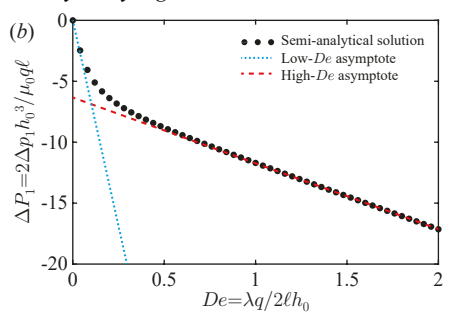


FIGURE 7. Non-dimensional pressure drop for the Oldroyd-B fluid in a contracting channel in the ultra-dilute limit. (a) Dimensionless pressure drop $\Delta P = \Delta p/(\mu_0 q \ell/2h_0^3)$ as a function of $De = \lambda q/(2\ell h_0)$ for $\tilde{\beta} = 0.05$. (b) First-order contribution $\Delta P_1 = \Delta p_1/(\mu_0 q \ell/2h_0^3)$ to the dimensionless pressure drop as a function of $De = \lambda q/(2\ell h_0)$. Gray triangles in (a) represent the results of the finite-element simulation. Black dots represent the semi-analytical solution (3.28). Cyan dotted lines represent the low-De asymptotic solution (3.32). Red dashed lines represent the high-De asymptotic solution (3.35). All calculations were performed using $H_{\ell} = 0.5$.

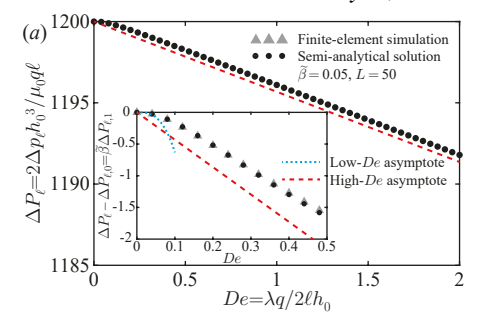
(gray triangles), showing very good agreement. The details of the numerical implementation in the finite-element software COMSOL Multiphysics are provided in Boyko & Stone (2022).

It is evident that the semi-analytical solution for the pressure drop in the contraction approaches the high-De asymptotic solution for $De \gtrsim 0.4$ and linearly decreases with the Deborah number. First, such an agreement for $De \gg 1$ is consistent with our results for the elastic stresses, shown in figure 3, and recent results of Hinch *et al.* (2023). Second, and more importantly, from the excellent agreement between the semi-analytical results and the high-De asymptotic solution, based on the components of the conformation tensor within the core flow region, we conclude that the viscoelastic boundary layer near the walls makes a negligible contribution to the pressure drop in the contracting channel.

Next, in figure 8(a) we present the non-dimensional pressure drop ΔP_{ℓ} in the exit channel as a function of De for $H_{\ell}=0.5$, $\tilde{\beta}=0.05$, and L=50. For De=2, a long exit channel of $L\gtrsim 30$ is required to reach the full relaxation of the elastic stresses and pressure gradient, consistent with (5.4). Figure 8(b) shows the first-order contribution $\Delta P_{\ell,1}$ as a function of De, which is independent of $\tilde{\beta}$. In contrast to the total pressure drop ΔP_{ℓ} , the first-order contribution $\Delta P_{\ell,1}$ does not depend on L, as shown in (4.2), provided that L is sufficiently long so that by the end of the exit channel the elastic stresses have achieved their fully relaxed values (2.16) with $H\equiv H_{\ell}$.

The inset in figure 8(a) shows a comparison of our semi-analytical predictions (black dots) and finite-element simulation results (gray triangles) for $\Delta P_{\ell} - \Delta P_{\ell,0} = \tilde{\beta} \Delta P_{\ell,1}$ as a function of De for $H_{\ell} = 0.5$, $\tilde{\beta} = 0.05$, and L = 5. We observe excellent agreement between the semi-analytical and numerical results. In addition, the low-De asymptotic solution (cyan dotted curve) accurately captures the numerical results for De < 0.05 and indicates that the pressure drop in the exit channel scales as De^3 for $De \ll 1$.

Similar to the contraction, the pressure drop in the exit channel linearly decreases with De for $De \gtrsim 0.3$, as shown in figure 8. While our semi-analytical solution linearly diminishes with the slope of -36/5, as predicted by the high-De asymptotic solution (red dashed lines), there is an offset between the two results for $\tilde{\beta}\Delta P_{\ell,1}$. In particular, for De = 0.4, we have a non-negligible relative error of approximately 30 %. However, the inset in figure 8(b) shows that as De increases, the agreement between our semi-analytical solution and the high-De asymptotic prediction significantly improves, resulting in relative errors of only approximately 5 % and 1 % for De = 2 and De = 10, respectively.



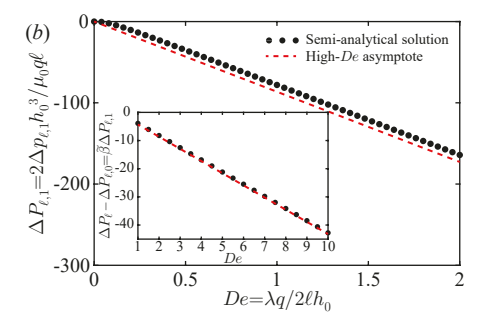


Figure 8. Non-dimensional pressure drop for the Oldroyd-B fluid in the exit channel of a contraction in the ultra-dilute limit. (a) Dimensionless pressure drop $\Delta P_\ell = \Delta p_\ell/(\mu_0 q\ell/2h_0^3)$ as a function of $De = \lambda q/(2\ell h_0)$ for $\tilde{\beta} = 0.05$ and L = 50. (b) First-order contribution $\Delta P_{\ell,1} = \Delta p_{\ell,1}/(\mu_0 q\ell/2h_0^3)$ to the dimensionless pressure drop as a function of $De = \lambda q/(2\ell h_0)$. Black dots represent the semi-analytical solutions (4.1) (ΔP_ℓ in (a)) and (4.2) ($\Delta P_{\ell,1}$ in (b)). The cyan dotted curve represents the low-De asymptotic solution (4.3). Red dashed lines represent the high-De asymptotic solution (4.4). The inset in (a) shows a comparison of semi-analytical predictions (black dots) and finite-element simulation results (gray triangles) for $\Delta P_\ell - \Delta P_{\ell,0} = \tilde{\beta} \Delta P_{\ell,1}$ as a function of De for $\tilde{\beta} = 0.05$ and L = 5. The inset in (b) shows $\Delta P_\ell - \Delta P_{\ell,0} = \tilde{\beta} \Delta P_{\ell,1}$ as a function of De for $\tilde{\beta} = 0.05$ in range of $1 \leqslant De \leqslant 10$. All calculations were performed using $H_\ell = 0.5$. $\Delta P_\ell = 2\Delta p_\ell h_0^3/\mu_0 q\ell$ and $\Delta P_{\ell,1} = 2\Delta p_{\ell,1} h_0^3/\mu_0 q\ell$.

We note that our theoretical approach, based on the ultra-dilute limit, allows us to study the behavior of the elastic stresses and pressure drop at arbitrary values of De. In particular, we can predict the behavior in the high-Deborah-number regime, for example, De = 2 and even De = 10, which we are currently unable to access via finite-element simulations. Note, however, that we have assumed steady flows, so further investigation would be required to assess whether there might be flow instabilities at higher De.

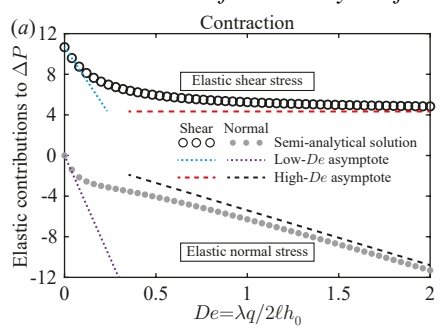
5.4. Different contributions to the pressure drop in the contraction and exit channel

In the previous subsection, we observed a monotonic reduction in the dimensionless pressure drop with increasing De for an Oldroyd-B fluid flowing through the contraction and exit channel (figures 7 and 8). To understand the source of such pressure drop reduction, we elucidate the relative importance of elastic contributions to the pressure drop.

The elastic contributions to the non-dimensional pressure drop across the contraction and exit channel, scaled by $\tilde{\beta}$, as a function of De are shown in figures 9(a) and 9(b), respectively. Black circles and gray dots represent the elastic shear and normal stress contributions obtained from the semi-analytical solutions (3.28) and (4.1). Cyan dotted and purple curves represent the elastic shear and normal stress contributions obtained from the low-De asymptotic solutions (3.32) and (4.3). Red and black dashed lines represent the elastic shear and normal stress contributions obtained from the high-De asymptotic solutions (3.35) and (4.4). As expected based on our previous results, we observe excellent agreement between our low-and high-De asymptotic solutions and the semi-analytical predictions.

The first main source for the pressure drop reduction is the elastic normal stress contribution, which linearly decreases with De in the contraction and exit channel at low and high Deborah numbers. As noted by Hinch *et al.* (2023), this is because the elastic normal stresses, which correspond to the tension in the streamlines, are higher at the end of the contraction (exit channel) compared with the beginning of the contraction (exit channel). These higher elastic normal stresses pull the fluid along and thus require less pressure to push.

The second main source for the pressure drop reduction is the decrease of elastic shear stress contribution with De due to the long time (or long distance) required for the elastic



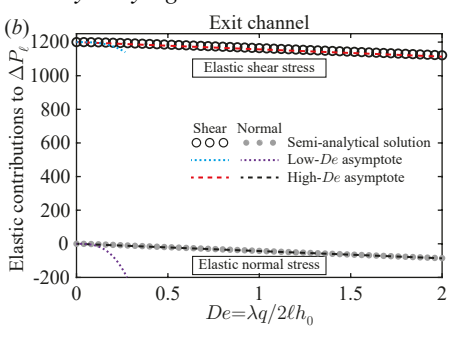


FIGURE 9. Elastic contributions to the non-dimensional pressure drop of the Oldroyd-B fluid, scaled by $\hat{\beta}$, in (a) the contraction and (b) the exit channel in the ultra-dilute limit. Black circles and gray dots represent the semi-analytical solutions (3.28) (contraction) and (4.1) (exit channel) for elastic shear and normal stress contributions. Cyan dotted and purple curves represent the low-De asymptotic solutions (3.32) (contraction) and (4.3) (exit channel) for elastic shear and normal stress contributions. Red and black dashed lines represent the high-De asymptotic solutions (3.35) (contraction) and (4.4) (exit channel) for elastic shear and normal stress contributions. All calculations were performed using $H_{\ell} = 0.5$ and L = 50.

shear stresses to approach their eventual relaxed values far downstream. As a result, the elastic shear stresses are lower than the fully relaxed value $\tilde{A}_{12} = -3De\eta/H_{\ell}^2$ (see figure 3), and their contribution to the pressure drop is smaller than the steady Poiseuille value of $3\tilde{\beta} \int_0^1 H(Z)^{-3} dZ$ (contraction) and $3\tilde{\beta} L/H_\ell^3$ (exit channel), thus reducing the pressure drop. At low Deborah numbers, such a decrease scales as De and De^3 for a smooth contraction and exit channel, respectively. However, at high Deborah numbers, it approaches a constant asymptotic value of $3\tilde{\beta} \int_0^1 H(Z)^{-1} dZ$ for the contraction. For the exit channel, $\Delta P_{\ell,1}^{SS}$ linearly depends on the Deborah number since the relaxation of the elastic shear stresses occurs over the distance L, which scales linearly with De, as shown in (5.4).

6. Concluding remarks

In this work, we applied the lubrication approximation and considered the ultra-dilute limit to study the flow of an Oldroyd-B fluid in arbitrarily shaped contracting channels. Specifically, we exploited the one-way coupling between the parabolic velocity and polymer conformation tensor in the ultra-dilute limit to derive closed-form expressions for the microstructure deformation and the flow rate–pressure drop relation for arbitrary values of the Deborah number. We provided analytical expressions for the conformation tensor and the $q-\Delta p$ relation in the low- and high-Deborah-number limits for the contraction and exit channels, complementing the asymptotic results of Boyko & Stone (2022) and the analysis of Hinch et al. (2023) at any concentration. We further analyzed the viscoelastic boundary layer of thickness $O(De^{-1})$, existing near the walls at high Deborah numbers, and derived the boundary-layer asymptotic solutions. We validated our semi-analytical and asymptotic results for the pressure drop in the smooth contraction and exit channels with 2-D finite-element numerical simulations and found excellent agreement.

For both contraction and exit channels, the pressure drop of an Oldroyd-B fluid monotonically decreases with increasing De and scales linearly with De at high Deborah numbers, as shown in figures 7 and 8. We identified two mechanisms for such pressure drop reduction (see figure 9). The first is higher elastic normal stresses at the end of the contraction and exit channels, relative to the corresponding entry values, that pull the fluid along and thus require less pressure to push. The second source for the pressure drop reduction is because, once perturbed from their upstream values, the elastic shear stresses require a long distance to

725

726

727

728

729 730

731

732

733

734 735

736 737

738

739

740

741

742

743

744

745

746

747

748

749 750

751

760

766

769

approach their new downstream fully relaxed values, as shown in figure 3, so again reducing the pressure drop.

Our theoretical approach, which relies on lubrication theory and the ultra-dilute limit, allows us to study the behavior of the elastic stresses and pressure drop of an Oldroyd-B fluid at arbitrary values of De. Our theory is not restricted to the case of 2-D contracting channels and can be utilized to study different slowly varying geometries, such as expansions and constrictions. The approach can also be extended to axisymmetric geometries. Furthermore, the theoretical framework we presented enables us to access sufficiently high Deborah numbers, which are difficult and sometimes impossible to study via numerical simulations due to the high-Weissenberg-number problem (Owens & Phillips 2002; Alves $et\ al.\ 2021$). We, therefore, believe that our analytical and semi-analytical results for the ultra-dilute limit are of fundamental importance as they may serve for simulation validation.

Finally, we note that our theoretical predictions for the pressure drop reduction of an Oldroyd-B fluid in a contraction are consistent with the previous numerical reports on 2-D abruptly contracting geometries (Aboubacar et al. 2002; Alves et al. 2003; Binding et al. 2006; Aguayo et al. 2008). However, these predictions are opposite to the experiments showing a nonlinear increase in the pressure drop with De for the flow of a Boger fluid through abrupt axisymmetric contraction-expansion and contraction geometries (Rothstein & McKinley 1999, 2001; Nigen & Walters 2002; Sousa et al. 2009). As noted by Alves et al. (2003) and Hinch et al. (2023), this discrepancy might be attributed to the lack of dissipative effects in the Oldroyd-B model. Thus, as a future research direction, it is interesting to study more complex constitutive equations, such as a finitely extensible nonlinear elastic (FENE) model introduced by Chilcott & Rallison (1988) (FENE-CR) and a finitely extensible nonlinear elastic model with the Peterlin approximation (FENE-P), that incorporate dissipation and additional microscopic features of polymer solutions and understand how these features affect the pressure drop. We anticipate that even for a more complex constitutive model, the theoretical framework presented here will enable the development of a simplified, reducedorder theory, allowing us to study the behavior at non-small Deborah numbers.

- Funding. E.B. acknowledges the support by grant no. 2022688 from the US-Israel Binational Science Foundation (BSF). H.A.S. acknowledges the support from grant no. CBET-2246791 from the United States
- 754 National Science Foundation (NSF).
- 755 **Declaration of interests.** The authors report no conflict of interest.
- 756 Author ORCIDs.
- 757 Evgeniy Boyko https://orcid.org/0000-0002-9202-5154;
- 758 John Hinch https://orcid.org/0000-0003-3130-7761;
- 759 Howard A. Stone https://orcid.org/0000-0002-9670-0639.

Appendix A. Orthogonal curvilinear coordinates for a slowly varying geometry

In this appendix, we provide additional details for orthogonal curvilinear coordinates for a slowly varying geometry used in our theoretical analysis. We consider a slowly spatially varying channel with a given shape h that varies on the length scale ℓ , so that $h = h(z/\ell) = h_0H(Z)$. We transform the Cartesian coordinates (Z, Y) to curvilinear coordinates (ξ, η) with the mapping

$$\xi = Z + \epsilon^2 Q(Z, Y), \qquad \eta = \frac{Y}{H(Z)},$$
 (A1)

where $Z = z/\ell$, $Y = y/h_0$, and Q is an unknown function yet to be determined. Note that, in the lubrication limit, the orthogonal coordinate ξ (scaled by ℓ) is nearly in the z-direction.

We find Q(Z,Y) by requiring that the curvilinear coordinates (ξ,η) are orthogonal, i.e.,

770 $\nabla \xi \cdot \nabla \eta = 0$. Using the relations

771
$$\nabla \xi = \left[\epsilon \frac{\partial \xi}{\partial Z}, \frac{\partial \xi}{\partial Y} \right] = \left[\epsilon \left(1 + \epsilon^2 \frac{\partial Q}{\partial Z} \right), \epsilon^2 \frac{\partial Q}{\partial Y} \right], \tag{A 2a}$$

772

790

$$\nabla \eta = \left[\epsilon \frac{\partial \eta}{\partial Z}, \frac{\partial \eta}{\partial Y} \right] = \left[-\epsilon \frac{Y H'(Z)}{H(Z)^2}, \frac{1}{H(Z)} \right], \tag{A 2b}$$

774 we obtain

775
$$\nabla \xi \cdot \nabla \eta = \frac{\epsilon^2}{H(Z)} \left[-\left(1 + \epsilon^2 \frac{\partial Q}{\partial Z}\right) \frac{YH'(Z)}{H(Z)} + \frac{\partial Q}{\partial Y} \right]. \tag{A 3}$$

776 Therefore, $\nabla \xi \cdot \nabla \eta = O(\epsilon^4)$ provided we set

777
$$\frac{\partial Q}{\partial Y} = \frac{YH'(Z)}{H(Z)} \Rightarrow Q(Z,Y) = -\frac{1}{2}\frac{H'(Z)}{H(Z)}(H(Z)^2 - Y^2), \tag{A4}$$

where without loss of generality, we choose $Q \equiv 0$ on Y = H(Z). Hence, the orthogonal curvilinear coordinates (ξ, η) are

780
$$\xi = Z - \frac{1}{2}\epsilon^2 \frac{H'(Z)}{H(Z)} (H(Z)^2 - Y^2) + O(\epsilon^4), \qquad \eta = \frac{Y}{H(Z)}. \tag{A 5}$$

Using (A 5), the inverse transformation is (see also Hinch et al. 2023)

782
$$Z = \xi + \frac{1}{2}\epsilon^2 H'(\xi)H(\xi)(1 - \eta^2) + O(\epsilon^4) = \xi + \frac{1}{4}(H(\xi)^2)'(1 - \eta^2) + O(\epsilon^4), \quad (A 6a)$$
783

$$Y(\xi, \eta) = \eta H(\xi), \tag{A 6b}$$

where evaluating $H(\xi)$ rather than H(Z) introduces a relative error of $O(\epsilon^2)$.

In what follows, it is also convenient to use the dimensional form of the transformation (A6), given as

788
$$z = \bar{\xi} + \frac{1}{2}\epsilon h_0 \frac{dH(\xi)}{d\xi} H(\xi) (1 - \eta^2) + O(\epsilon^4), \qquad y = \eta h_0 H(\xi), \tag{A 7}$$

789 where we have defined the dimensional coordinate $\bar{\xi} = \xi \ell$.

A.1. Curvilinear orthonormal basis vectors

The expressions for the curvilinear orthonormal basis vectors \mathbf{e}_{ξ} and \mathbf{e}_{η} in terms of \mathbf{e}_{z} and \mathbf{e}_{y} are obtained from

793
$$\mathbf{e}_{\xi} = \frac{\partial \mathbf{x}}{\partial \bar{\xi}} \frac{1}{|\partial \mathbf{x}/\partial \bar{\xi}|}, \qquad \mathbf{e}_{\eta} = \frac{\partial \mathbf{x}}{\partial \eta} \frac{1}{|\partial \mathbf{x}/\partial \eta|}, \tag{A 8}$$

794 where using (A7), we have

795
$$\frac{\partial \mathbf{x}}{\partial \bar{\xi}} = \left(\frac{\partial z}{\partial \bar{\xi}}, \frac{\partial y}{\partial \bar{\xi}}\right) = \left(1 + O(\epsilon^2), h_0 \frac{\mathrm{d}H(\xi)}{\mathrm{d}\bar{\xi}}\eta\right) = \left(1 + O(\epsilon^2), \epsilon \frac{\mathrm{d}H(\xi)}{\mathrm{d}\xi}\eta\right), \quad (A 9a)$$

797
$$\frac{\partial \mathbf{x}}{\partial \eta} = \left(\frac{\partial z}{\partial \eta}, \frac{\partial y}{\partial \eta}\right) = \left(-\epsilon h_0 \frac{\mathrm{d}H(\xi)}{\mathrm{d}\xi} H(\xi) \eta, h_0 H(\xi)\right),\tag{A 9b}$$

and $h_{\xi} = \left| \partial x / \partial \bar{\xi} \right| \approx 1$ and $h_{\eta} = \left| \partial x / \partial \eta \right| \approx h_0 H(\xi) = h(\bar{\xi}/\ell)$ are the metric coefficients (or scale factors) in the ξ - and η -directions, respectively, with small corrections of $O(\epsilon^2)$.

Substituting (A 9) into (A 8), we obtain

801
$$\mathbf{e}_{\mathcal{E}} \approx \mathbf{e}_{z} + \epsilon H'(\xi) \eta \mathbf{e}_{y}, \qquad \mathbf{e}_{n} \approx -\epsilon H'(\xi) \eta \mathbf{e}_{z} + \mathbf{e}_{y}. \tag{A 10}$$

802 A.2. Velocity and conformation tensor in Cartesian and curvilinear coordinates

The velocity field and the conformation tensor can be expressed either in Cartesian or curvilinear coordinates. Specifically, the velocity $\mathbf{u} = u_z \mathbf{e}_z + u_y \mathbf{e}_y$ in Cartesian coordinates is related to the velocity $\mathbf{u} = u \mathbf{e}_{\xi} + v \mathbf{e}_{\eta}$ in curvilinear coordinates through (Brand 1947)

$$\begin{pmatrix} u_z \\ u_y \end{pmatrix} = \mathbf{M} \cdot \begin{pmatrix} u \\ v \end{pmatrix}, \tag{A 11}$$

where \mathbf{M} is the coordinate transformation matrix obtained from (A 10) and given as

808
$$\mathbf{M} = \begin{pmatrix} 1 & -\epsilon H'(\xi)\eta \\ \epsilon H'(\xi)\eta & 1 \end{pmatrix}. \tag{A 12}$$

We introduce non-dimensional velocity components in curvilinear coordinates, similar to the non-dimensionalization (2.5a),

811
$$U = \frac{u}{u_c}, \qquad V = \frac{v}{\epsilon u_c}. \tag{A 13}$$

Using (A 11)–(A 13) provides the relations between non-dimensional velocity components

813 in different coordinates

814
$$U_z = U - \epsilon^2 \eta H'(\xi) V, \qquad U_v = \eta H'(\xi) U + V.$$
 (A 14)

- While velocity in the z- and ξ -directions are the same, albeit to a $O(\epsilon^2)$ correction, the
- velocity in the y-direction is greater by $\eta H'(\xi)U$ than the velocity in the η -direction.
- Similarly, the conformation tensor $\mathbf{A} = A_{zz}\mathbf{e}_z\mathbf{e}_z + A_{zy}(\mathbf{e}_z\mathbf{e}_y + \mathbf{e}_y\mathbf{e}_z) + A_{yy}\mathbf{e}_y\mathbf{e}_y$ in Cartesian coordinates is related to the conformation tensor $\mathbf{A} = A_{11}\mathbf{e}_{\xi}\mathbf{e}_{\xi} + A_{12}(\mathbf{e}_{\xi}\mathbf{e}_{\eta} + \mathbf{e}_{\eta}\mathbf{e}_{\xi}) + A_{22}\mathbf{e}_{\eta}\mathbf{e}_{\eta}$
- in curvilinear coordinates through (Brand 1947)

$$\begin{pmatrix} A_{zz} & A_{zy} \\ A_{yz} & A_{yy} \end{pmatrix} = \mathbf{M} \cdot \begin{pmatrix} A_{11} & A_{12} \\ A_{21} & A_{22} \end{pmatrix} \cdot \mathbf{M}^{\mathrm{T}}.$$
 (A 15)

Next, we define scaled \tilde{A}_{11} , \tilde{A}_{12} , and \tilde{A}_{22} in curvilinear coordinates, similar to the non-

822 dimensionalization (2.5c),

823
$$\tilde{A}_{11} = \epsilon^2 A_{11}, \qquad \tilde{A}_{12} = \epsilon A_{12}, \qquad \tilde{A}_{22} = A_{22}.$$
 (A 16)

Finally, using (A 12) and (A 15)–(A 16), we obtain the relations between conformation tensor

825 components in different coordinates

826
827
$$\tilde{A}_{zz} = \tilde{A}_{11} + O(\epsilon^2),$$
 (A 17a)

$$\tilde{A}_{zy} = \tilde{A}_{12} + \eta H'(\xi) \tilde{A}_{11} + O(\epsilon^2), \tag{A 17b}$$

830
$$\tilde{A}_{yy} = \tilde{A}_{22} + 2\eta H'(\xi)\tilde{A}_{12} + \eta^2 (H'(\xi))^2 \tilde{A}_{11} + O(\epsilon^2). \tag{A 17c}$$

Appendix B. Low- $\tilde{\beta}$ lubrication analysis in the exit channel: detailed derivation

- We here provide details of the derivation of closed-form expressions for the conformation
- tensor and the pressure drop in the uniform exit channel for $\hat{\beta} \ll 1$.
- B.1. Velocity, conformation, and pressure drop in the exit channel at the leading order in $\tilde{\beta}$ The velocity field and pressure drop in the exit channel at the leading order in $\tilde{\beta}$ are

$$U_0 = \frac{3}{2} \frac{1}{H_\ell} (1 - \eta^2), \qquad V_0 \equiv 0, \qquad \Delta P_{\ell,0} = \frac{3L}{H_\ell^3}.$$
 (B1a - c)

As expected, (B 1) simply represents the solution for the velocity and pressure drop of a Newtonian fluid with a constant viscosity μ_0 flowing in a straight channel of (non-dimensional) height H_{ℓ} and length L.

Substituting (B 1a) into (3.6), we obtain the governing equations for the conformation tensor components in the exit channel at the leading order in $\tilde{\beta}$,

840
$$U_0 \frac{\partial \tilde{A}_{22,0}}{\partial Z} = -\frac{1}{De} (\tilde{A}_{22,0} - 1), \tag{B 2a}$$

842
$$U_0 \frac{\partial \tilde{A}_{12,0}}{\partial Z} - \frac{1}{H_\ell} \frac{dU_0}{d\eta} \tilde{A}_{22,0} = -\frac{1}{De} \tilde{A}_{12,0}, \tag{B 2b}$$

844

849

856

857

858

859

860

861

862

863

868

$$U_0 \frac{\partial \tilde{A}_{11,0}}{\partial Z} - \frac{2}{H_{\ell}} \frac{dU_0}{d\eta} \tilde{A}_{12,0} = -\frac{1}{De} \tilde{A}_{11,0}.$$
 (B 2c)

Equations (B 2), similar to (3.6), represent a set of one-way coupled first-order semi-linear partial differential equations that can be solved first for $\tilde{A}_{22,0}$, followed by $\tilde{A}_{12,0}$, and then for $\tilde{A}_{11,0}$. The solution of these equations is

848
$$\tilde{A}_{22,0} = 1 + (\tilde{A}_{22,0}^{\text{ref}}(\eta) - 1)e^{-2H_{\ell}Z_{\ell}/[3De(1-\eta^2)]}, \tag{B 3}$$

850
$$\tilde{A}_{12,0} = -\frac{3De}{H_{\ell}^2} \eta + e^{-2H_{\ell}Z_{\ell}/[3De(1-\eta^2)]} \left[\tilde{A}_{12,0}^{\text{ref}}(\eta) + \frac{3De}{H_{\ell}^2} \eta - \frac{2\eta(\tilde{A}_{22,0}^{\text{ref}}(\eta) - 1)Z_{\ell}}{H_{\ell}(1-\eta^2)} \right], \quad (B4)$$

852
$$\tilde{A}_{11,0} = \frac{18De^2}{H_{\ell}^4} \eta^2 + e^{-2H_{\ell}Z_{\ell}/[3De(1-\eta^2)]} \left[\tilde{A}_{11,0}^{\text{ref}}(\eta) - \frac{18De^2}{H_{\ell}^4} \eta^2 + \frac{4\eta^2 (\tilde{A}_{22,0}^{\text{ref}}(\eta) - 1)Z_{\ell}^2}{H_{\ell}^2 (1-\eta^2)^2} - \frac{4\eta Z_{\ell} [3De\eta + H_{\ell}^2 \tilde{A}_{12,0}^{\text{ref}}(\eta)]}{H_{\ell}^3 (1-\eta^2)} \right], \tag{B 5}$$

where $Z_{\ell}=Z-1$ and $\tilde{A}^{\rm ref}_{22,0}(\eta)=\tilde{A}_{22,0}(Z=1,\eta),$ $\tilde{A}^{\rm ref}_{12,0}(\eta)=\tilde{A}_{12,0}(Z=1,\eta),$ and $\tilde{A}^{\rm ref}_{11,0}(\eta)=\tilde{A}_{11,0}(Z=1,\eta)$ are the reference distributions of the conformation tensor components at the

outlet (Z = 1) of the non-uniform channel that can be obtained from (3.8), (3.9), and (3.10). We note that, under the assumption of a fully developed flow in the entire exit channel so that $U(\eta) = (3/2H_{\ell})(1 - \eta^2)$, the governing equations for the conformation tensor components (B 2) and their solution (B 3)–(B 5) are valid not only at $O(\tilde{\beta}^0)$ but for arbitrary values of $\tilde{\beta}$.

Finally, we note that the components of the conformation tensor at the walls of the exit channel $(\eta = \pm 1)$ are given in (3.12), with $H(Z) \equiv H_{\ell}$. Thus, the conformation tensor components at the walls of the exit channel attain their fully relaxed values without spatial development.

864 B.1.1. Conformation tensor in the exit channel at low De numbers

At low Deborah numbers, we use (3.13) to obtain the reference distributions of the conformation tensor components at the beginning of the exit channel,

867
$$\tilde{A}_{22,0}^{\text{ref}}(\eta) = 1 - \frac{9De^2H''(1)}{2H_{\ell}^3}(1 - \eta^2)^2, \tag{B 6a}$$

869
$$\tilde{A}_{12,0}^{\text{ref}}(\eta) = -\frac{3De}{H_{\ell}^2} \eta + \frac{81De^3 H''(1)}{2H_{\ell}^5} \eta (1 - \eta^2)^2, \tag{B 6b}$$

876

881

896

871
$$\tilde{A}_{11,0}^{\text{ref}}(\eta) = \frac{18De^2}{H_{\ell}^4} \eta^2 - \frac{486De^4H''(1)}{H_{\ell}^7} \eta^2 (1 - \eta^2)^2, \tag{B 6c}$$

where, for a smooth geometry, we have assumed that H'(1) = H'''(1) = 0.

Substituting (B 6) into (B 3), we obtain explicit expressions for the spatial relaxation of the conformation tensor components in the exit channel for $De \ll 1$,

875
$$\tilde{A}_{22,0} = 1 - \frac{9De^2H''(1)}{2H_{\ell}^3} (1 - \eta^2)^2 e^{-2H_{\ell}Z_{\ell}/[3De(1 - \eta^2)]}, \tag{B7}a)$$

877 $\tilde{A}_{12,0} = -\frac{3De}{H_{\ell}^2} \eta + \frac{9De^2 H''(1)}{H_{\ell}^4} \eta (1 - \eta^2) e^{-2H_{\ell} Z_{\ell}/[3De(1 - \eta^2)]} \left[\frac{9De}{2H_{\ell}} (1 - \eta^2) + Z_{\ell} \right], \quad (B7b)$

879
$$\tilde{A}_{11,0} = \frac{18De^2}{H_{\ell}^4} \eta^2 - \frac{18De^2H''(1)}{H_{\ell}^5} \eta^2 e^{-2H_{\ell}Z_{\ell}/[3De(1-\eta^2)]} \left[\frac{27De^2}{H_{\ell}^2} (1-\eta^2)^2 + Z_{\ell}^2 + \frac{9De}{H_{\ell}} Z_{\ell} (1-\eta^2) \right].$$
(B7c)

882 B.1.2. Conformation tensor in the exit channel at high De numbers

From (3.15), (3.17), and (3.19) it follows that the reference distributions of the conformation

tensor components at the beginning of the exit channel within the core flow region in the

885 high-De limit are

886
$$\tilde{A}_{22,0}^{\text{ref}}(\eta) = H_{\ell}^2, \qquad \tilde{A}_{12,0}^{\text{ref}}(\eta) = -3De\eta, \qquad \tilde{A}_{11,0}^{\text{ref}}(\eta) = \frac{18De^2}{H_{\ell}^2}\eta^2.$$
 (B 8)

Substituting (B 8) into (B 3) provides expressions for the spatial relaxation of the conformation tensor components in the exit channel for $De \gg 1$,

889
$$\tilde{A}_{22,0} = 1 + (H_{\ell}^2 - 1)e^{-2H_{\ell}Z_{\ell}/[3De(1-\eta^2)]},$$
 (B 9a)

891
$$\tilde{A}_{12,0} = -\frac{3De\eta}{H_{\ell}^2} + e^{-2H_{\ell}Z_{\ell}/[3De(1-\eta^2)]} \left[-3De\eta + \frac{3De\eta}{H_{\ell}^2} + \frac{2\eta(1-H_{\ell}^2)Z_{\ell}}{H_{\ell}(1-\eta^2)} \right], \quad (B9b)$$

893
$$\tilde{A}_{11,0} = \frac{18De^{2}\eta^{2}}{H_{\ell}^{4}} + e^{-2H_{\ell}Z_{\ell}/[3De(1-\eta^{2})]} \left[\frac{18De^{2}\eta^{2}}{H_{\ell}^{2}} - \frac{18De^{2}\eta^{2}}{H_{\ell}^{4}} + \frac{4\eta^{2}(H_{\ell}^{2} - 1)Z_{\ell}^{2}}{H_{\ell}^{2}(1 - \eta^{2})^{2}} - \frac{12De\eta^{2}Z_{\ell}(1 - H_{\ell}^{2})}{H_{\ell}^{3}(1 - \eta^{2})} \right].$$
894 (B 9c)

B.2. Pressure drop in the exit channel at the first order in $\tilde{\beta}$

Using (2.21) and (3.27), the expressions for the pressure drop at $O(\tilde{\beta})$, $\Delta P_{\ell,1}$, and the total pressure drop in the exit channel up to $O(\tilde{\beta})$, ΔP_{ℓ} , are

899
$$\Delta P_{\ell,1} = -\frac{3L}{H_{\ell}^3} + \frac{3}{2De} \int_0^1 (1 - \eta^2) \left[\tilde{A}_{11,0} \right]_{Z_{\ell} = L}^{Z_{\ell} = 0} d\eta + \frac{3}{DeH_{\ell}} \int_0^1 \eta \left[\int_L^0 \tilde{A}_{12,0} dZ_{\ell} \right] d\eta, \quad (B 10)$$

900 and

901

910

$$\Delta P_{\ell} = \underbrace{(1 - \tilde{\beta}) \frac{3L}{H_{\ell}^{3}}}_{\text{Solvent stress}} + \underbrace{\frac{3\tilde{\beta}}{2De} \int_{0}^{1} (1 - \eta^{2}) \left[\tilde{A}_{11,0}\right]_{Z_{\ell} = L}^{Z_{\ell} = 0} d\eta}_{\text{Elastic normal stress}} + \underbrace{\frac{3\tilde{\beta}}{DeH_{\ell}} \int_{0}^{1} \eta \left[\int_{L}^{0} \tilde{A}_{12,0} dZ_{\ell}\right] d\eta}_{\text{Elastic shear stress}},$$

(B 11)

where $\tilde{A}_{11,0}$ and $\tilde{A}_{12,0}$ are given in (B 4) and (B 5) and $\left[\tilde{A}_{11,0}\right]_{Z_{\ell}=L}^{Z_{\ell}=0} = \tilde{A}_{11,0}(Z_{\ell}=0,\eta) - \tilde{A}_{11,0}(Z_{\ell}=L,\eta)$. The three terms on the right-hand side of (B 11) represent, respectively, the

Newtonian solvent stress contribution, the elastic normal stress contribution, and the elastic

shear stress contribution to the pressure drop.

It is possible to express the first-order contribution $\Delta P_{\ell,1}$ in terms of the difference between the conformation tensor components at the beginning and end of the exit channel. First, integrating (B 2a) and (B 2b) with respect to Z_{ℓ} from L to 0, we obtain

909
$$U_0 \left[\tilde{A}_{22,0} \right]_{Z_{\ell}=L}^{Z_{\ell}=0} = -\frac{1}{De} \int_{L}^{0} (\tilde{A}_{22,0} - 1) dZ_{\ell}, \tag{B 12}$$

911 $U_0 \left[\tilde{A}_{12,0} \right]_{Z_{\ell}=L}^{Z_{\ell}=0} - \frac{1}{H_{\ell}} \frac{dU_0}{d\eta} \int_{L}^{0} \tilde{A}_{22,0} dZ_{\ell} = -\frac{1}{De} \int_{L}^{0} \tilde{A}_{12,0} dZ_{\ell}. \tag{B 13}$

912 Substituting (B 12) into (B 13) yields

913
$$U_0 \left[\tilde{A}_{12,0} \right]_{Z_{\ell}=L}^{Z_{\ell}=0} + \frac{De}{H_{\ell}} \frac{dU_0}{d\eta} U_0 \left[\tilde{A}_{22,0} \right]_{Z_{\ell}=L}^{Z_{\ell}=0} + \frac{L}{H_{\ell}} \frac{dU_0}{d\eta} = -\frac{1}{De} \int_{L}^{0} \tilde{A}_{12,0} dZ_{\ell}.$$
 (B 14)

Thus, using (B 14), the last term on the right-hand side of (B 11) can be expressed as

915
$$\frac{3}{DeH_{\ell}} \int_{0}^{1} \eta \left[\int_{L}^{0} \tilde{A}_{12,0} dZ_{\ell} \right] d\eta = -\frac{9}{2H_{\ell}^{2}} \int_{0}^{1} \eta (1 - \eta^{2}) \left[\tilde{A}_{12,0} \right]_{Z_{\ell}=L}^{Z_{\ell}=0} d\eta$$

$$+ \frac{27De}{2H_{\ell}^{4}} \int_{0}^{1} \eta^{2} (1 - \eta^{2}) \left[\tilde{A}_{22,0} \right]_{Z_{\ell}=L}^{Z_{\ell}=0} d\eta + \frac{3L}{H_{\ell}^{3}}. (B 15)$$

Substituting (B 15) into (B 11) provides the alternative expression for $\Delta P_{\ell,1}$,

918
$$\Delta P_{\ell,1} = \frac{3}{2De} \int_0^1 (1 - \eta^2) \left[\tilde{A}_{11,0} \right]_{Z_{\ell}=L}^{Z_{\ell}=0} d\eta - \frac{9}{2H_{\ell}^2} \int_0^1 \eta (1 - \eta^2) \left[\tilde{A}_{12,0} \right]_{Z_{\ell}=L}^{Z_{\ell}=0} d\eta$$
919
$$+ \frac{27De}{2H_{\ell}^4} \int_0^1 \eta^2 (1 - \eta^2) \left[\tilde{A}_{22,0} \right]_{Z_{\ell}=L}^{Z_{\ell}=0} d\eta. \tag{B 16}$$

- Under the assumption that L is such that the elastic stresses reach their fully relaxed values by
- the end of the exit channel, (B 16) shows that the first-order contribution $\Delta P_{\ell,1}$ is independent
- of L since the steady-state values of $\tilde{A}_{11,0}$, $\tilde{A}_{12,0}$, and $\tilde{A}_{22,0}$ depend solely on the η coordinate.
- 923 B.2.1. Pressure drop in the exit channel at $O(\tilde{\beta})$ in the low-De limit
- To calculate the pressure drop ΔP_{ℓ} in the exit channel at low Deborah numbers, we use
- 925 (B7b)-(B7c) and (B10). The elastic normal stress contribution to $\Delta P_{\ell,1}$ is

926
$$\Delta P_{\ell,1}^{\text{NS}} = \frac{3}{2De} \int_0^1 (1 - \eta^2) \left[\tilde{A}_{11,0} \right]_{Z_{\ell} = L}^{Z_{\ell} = 0} d\eta = -\frac{1296De^3 H''(1)}{35 H_{\ell}^7} \quad \text{for} \quad De \ll 1. \quad (B 17)$$

The elastic shear stress contribution to the pressure drop at $O(\tilde{\beta})$ is

928
$$\Delta P_{\ell,1}^{SS} = \frac{3}{DeH_{\ell}} \int_{0}^{1} \eta \left[\int_{L}^{0} \tilde{A}_{12,0} dZ_{\ell} \right] d\eta, \tag{B 18}$$

929 with the integral $\int_{I}^{0} \tilde{A}_{12,0} dZ_{\ell}$ given as

930
$$\int_{L}^{0} \tilde{A}_{12,0} dZ_{\ell} \approx \frac{3DeL}{H_{\ell}^{2}} \eta - \frac{81De^{4}H''(1)}{H_{\ell}^{6}} \eta (1 - \eta^{2})^{3} \quad \text{for} \quad De \ll 1,$$
 (B 19)

- where we have neglected terms multiplying $e^{-2H_\ell L/[3De(1-\eta^2)]} \approx 0$.
- 932 Substituting (B 19) into (B 18), we obtain

933
$$\Delta P_{\ell,1}^{SS} = \frac{3L}{H_{\ell}^3} - \frac{432De^3H''(1)}{35H_{\ell}^7} \quad \text{for} \quad De \ll 1.$$
 (B 20)

Combining the normal and shear stress contributions, (B 17) and (B 20), provides the expression for the pressure drop at $O(\tilde{\beta})$ in the low-De limit

936
$$\Delta P_{\ell,1} = -\frac{3L}{H_{\ell}^3} + \Delta P_{\ell,1}^{\text{NS}} + \Delta P_{\ell,1}^{\text{SS}} = -\frac{1728De^3H''(1)}{35H_{\ell}^7} \quad \text{for} \quad De \ll 1.$$
 (B 21)

937 Therefore, the total pressure drop in the exit channel in the low-De limit is

938
$$\Delta P_{\ell} = \underbrace{(1 - \tilde{\beta}) \frac{3L}{H_{\ell}^{3}}}_{\text{Solvent stress}} + \underbrace{-\frac{1296\tilde{\beta}De^{3}H''(1)}{35H_{\ell}^{7}}}_{\text{Elastic normal stress}} + \underbrace{\frac{3L}{H_{\ell}^{3}}\tilde{\beta} - \frac{432\tilde{\beta}De^{3}H''(1)}{35H_{\ell}^{7}}}_{\text{Elastic shear stress}}$$

$$= \frac{3L}{H_{\ell}^{3}} - \frac{1728\tilde{\beta}De^{3}H''(1)}{35H_{\ell}^{7}} \quad \text{for} \quad De \ll 1.$$
(B 22)

- Equation (B 22) shows that for a smooth contraction with H'(1) = H'''(1) = 0, the first non-
- vanishing viscoelastic contribution to the pressure drop in the exit channel at low Deborah
- numbers is only at $O(De^3)$ as the O(De) and $O(De^2)$ contributions are identically zero.
- 943 B.2.2. Pressure drop in the exit channel at $O(\tilde{\beta})$ in the high-De limit
- To calculate the pressure drop ΔP_{ℓ} in the exit channel at high Deborah numbers, we use
- 945 (B 9b)-(B 9c) and (B 10). The elastic normal stress contribution to $\Delta P_{\ell,1}$ is

946
$$\Delta P_{\ell,1}^{\text{NS}} = \frac{3}{2De} \int_0^1 (1 - \eta^2) \left[\tilde{A}_{11,0} \right]_{Z_{\ell} = L}^{Z_{\ell} = 0} d\eta = \frac{18}{5} De(H_{\ell}^{-2} - H_{\ell}^{-4}) \quad \text{for} \quad De \gg 1. \quad (B 23)$$

The elastic shear stress contribution to the pressure drop at $O(\tilde{\beta})$ is

$$\Delta P_{\ell,1}^{SS} = \frac{3}{DeH_{\ell}} \int_{0}^{1} \eta \left[\int_{L}^{0} \tilde{A}_{12,0} dZ_{\ell} \right] d\eta = \frac{3L}{H_{\ell}^{3}} + \frac{18}{5} De(H_{\ell}^{-2} - H_{\ell}^{-4}) \quad \text{for} \quad De \gg 1,$$
(B 24)

where the integral $\int_L^0 \tilde{A}_{12,0} dZ_\ell$, after neglecting terms multiplying $e^{-2H_\ell L/[3De(1-\eta^2)]} \approx 0$, is given as

951
$$\int_{L}^{0} \tilde{A}_{12,0} dZ_{\ell} \approx \frac{3DeL}{H_{\ell}^{2}} \eta + \frac{9De^{2}(H_{\ell}^{2} - 1)}{H_{\ell}^{3}} \eta (1 - \eta^{2}) \quad \text{for} \quad De \gg 1.$$
 (B 25)

Combining the normal and shear stress contributions, (B 23) and (B 24), provides the expression for the pressure drop at $O(\tilde{\beta})$ in the high-De limit

954
$$\Delta P_{\ell,1} = -\frac{3L}{H_{\ell}^3} + \Delta P_{\ell,1}^{\text{NS}} + \Delta P_{\ell,1}^{\text{SS}} = \frac{36}{5} De(H_{\ell}^{-2} - H_{\ell}^{-4}) \quad \text{for} \quad De \gg 1.$$
 (B 26)

Therefore, the total pressure drop in the exit channel in the high-De limit is

956
$$\Delta P_{\ell} = \underbrace{(1 - \tilde{\beta})\frac{3L}{H_{\ell}^{3}}}_{\text{Solvent stress}} + \underbrace{\frac{18}{5}\tilde{\beta}De(H_{\ell}^{-2} - H_{\ell}^{-4})}_{\text{Elastic normal stress}} + \underbrace{\frac{3L}{H_{\ell}^{3}}\tilde{\beta} + \frac{18}{5}\tilde{\beta}De(H_{\ell}^{-2} - H_{\ell}^{-4})}_{\text{Elastic shear stress}}$$

$$= \frac{3L}{H_{\ell}^{3}} + \frac{36}{5}\tilde{\beta}De(H_{\ell}^{-2} - H_{\ell}^{-4}) \quad \text{for} \quad De \gg 1. \tag{B 27}$$

REFERENCES

- ABOUBACAR, M., MATALLAH, H. & WEBSTER, M. F. 2002 Highly elastic solutions for Oldroyd-B and Phan-Thien/Tanner fluids with a finite volume/element method: planar contraction flows. *J. Non-Newtonian* Fluid Mech. **103** (1), 65–103.
- AGUAYO, J. P., TAMADDON-JAHROMI, H. R. & WEBSTER, M. F. 2008 Excess pressure-drop estimation in contraction and expansion flows for constant shear-viscosity, extension strain-hardening fluids. *J. Non-Newtonian Fluid Mech.* 153 (2-3), 157–176.
- Ahmed, H. & Biancofiore, L. 2021 A new approach for modeling viscoelastic thin film lubrication. J.
 Non-Newtonian Fluid Mech. 292, 104524.
- Ahmed, H. & Biancofiore, L. 2023 Modeling polymeric lubricants with non-linear stress constitutive
 relations. J. Non-Newtonian Fluid Mech. 321, 105123.
- ALVES, M. A., OLIVEIRA, P. J. & PINHO, F. T. 2003 Benchmark solutions for the flow of Oldroyd-B and PTT fluids in planar contractions. *J. Non-Newtonian Fluid Mech.* **110** (1), 45–75.
- ALVES, M. A., OLIVEIRA, P. J. & PINHO, F. T. 2021 Numerical methods for viscoelastic fluid flows. *Annu. Rev. Fluid Mech.* 53, 509–541.
- 972 ALVES, M. A. & POOLE, R. J. 2007 Divergent flow in contractions. *J. Non-Newtonian Fluid Mech.* **144** (2-3), 140–148.
- BECHERER, P., VAN SAARLOOS, W. & MOROZOV, A. N. 2009 Stress singularities and the formation of birefringent strands in stagnation flows of dilute polymer solutions. *J. Non-Newtonian Fluid Mech.* 157 (1-2), 126–132.
- 977 BINDING, D. M., PHILLIPS, P. M. & PHILLIPS, T. N. 2006 Contraction/expansion flows: The pressure drop and related issues. *J. Non-Newtonian Fluid Mech.* **137** (1-3), 31–38.
- 979 BIRD, R. B., ARMSTRONG, R. C. & HASSAGER, O. 1987 Dynamics of Polymeric Liquids, volume 1: Fluid Mechanics, 2nd edn. John Wiley and Sons.
- BOYKO, E. & STONE, H. A. 2021 Reciprocal theorem for calculating the flow rate–pressure drop relation for complex fluids in narrow geometries. *Phys. Rev. Fluids* **6**, L081301.
- BOYKO, E. & STONE, H. A. 2022 Pressure-driven flow of the viscoelastic Oldroyd-B fluid in narrow nonuniform geometries: analytical results and comparison with simulations. *J. Fluid Mech.* **936**, A23.
- 985 Brand, L. 1947 Vector and Tensor Analysis. John Wiley and Sons.
- 986 CHILCOTT, M. D. & RALLISON, J. M. 1988 Creeping flow of dilute polymer solutions past cylinders and spheres. *J. Non-Newtonian Fluid Mech.* **29**, 381–432.
- DANDEKAR, R. & ARDEKANI, A. M. 2021 Nearly touching spheres in a viscoelastic fluid. *Phys. Fluids* **33** (8), 083112.
- DATT, C. & Elfring, G. J. 2019 A note on higher-order perturbative corrections to squirming speed in
 weakly viscoelastic fluids. J. Non-Newtonian Fluid Mech. 270, 51–55.
- DATT, C., NASOURI, B. & ELFRING, G. J. 2018 Two-sphere swimmers in viscoelastic fluids. *Phys. Rev. Fluids* 3 (12), 123301.
- DATT, C., NATALE, G., HATZIKIRIAKOS, S. G. & ELFRING, G. J. 2017 An active particle in a complex fluid.
 J. Fluid Mech. 823, 675–688.

- Datta, S. S., Ardekani, A. M., Arratia, P. E., Beris, A. N., Bischofberger, I., McKinley, G. H.,
 Eggers, J. G., López-Aguilar, J. E., Fielding, S. M., Frishman, A., Graham, M. D., Guasto,
- 998 J. S., Haward, S. J., Shen, A. Q., Hormozi, S., Morozov, A., Poole, R. J., Shankar, V., Shaqfeh,
- 999 E. S. G., STARK, H., STEINBERG, V., SUBRAMANIAN, G. & STONE, H. A. 2022 Perspectives on viscoelastic flow instabilities and elastic turbulence. *Phys. Rev. Fluids* 7, 080701.
- Debbaut, B., Marchal, J. M. & Crochet, M. J. 1988 Numerical simulation of highly viscoelastic flows through an abrupt contraction. *J. Non-Newtonian Fluid Mech.* 29, 119–146.
- Ferrás, L. L., Afonso, A. M., Alves, M. A., Nóbrega, J. M. & Pinho, F. T. 2020 Newtonian and viscoelastic fluid flows through an abrupt 1: 4 expansion with slip boundary conditions. *Phys. Fluids* 32 (4), 043103.
- 1006 Gamaniel, S. S., Dini, D. & Biancofiore, L. 2021 The effect of fluid viscoelasticity in lubricated contacts 1007 in the presence of cavitation. *Tribol. Int.* **160**, 107011.
- 1008 GKORMPATSIS, S. D., GRYPARIS, E. A., HOUSIADAS, K. D. & BERIS, A. N. 2020 Steady sphere translation in a viscoelastic fluid with slip on the surface of the sphere. *J. Non-Newtonian Fluid Mech.* **275**, 104217.
- 1010 Hinch, E. J., Boyko, E. & Stone, H. A. 2023 Fast flow of an Oldroyd-B model fluid through a narrow slowly-varying contraction. *Submitted*.
- HOUSIADAS, K. D. & BERIS, A. N. 2023 Lubrication approximation of pressure-driven viscoelastic flow in a hyperbolic channel. *Phys. Fluids* **35** (12).
- HOUSIADAS, K. D., BINAGIA, J. P. & SHAQFEH, E. S. G. 2021 Squirmers with swirl at low Weissenberg number. *J. Fluid Mech.* **911**, A16.
- JAMES, D. F. & Roos, C. A. M. 2021 Pressure drop of a boger fluid in a converging channel. *J. Non-Newtonian Fluid Mech.* **293**, 104557.
- KEILLER, R. A. 1993 Spatial decay of steady perturbations of plane Poiseuille flow for the Oldroyd-B equation. *J. Non-Newtonian Fluid Mech.* **46** (2-3), 129–142.
- 1020 LARSON, R. G. 1988 Constitutive Equations for Polymer Melts and Solutions. Butterworths.
- 1021 LI, C., THOMASES, B. & GUY, R. D. 2019 Orientation dependent elastic stress concentration at tips of slender objects translating in viscoelastic fluids. *Phys. Rev. Fluids* **4** (3), 031301.
- Mokhtari, O., Latché, J.-C., Quintard, M. & Davit, Y. 2022 Birefringent strands drive the flow of viscoelastic fluids past obstacles. *J. Fluid Mech.* **948**, A2.
- Moore, M. N. J. & Shelley, M. J. 2012 A weak-coupling expansion for viscoelastic fluids applied to dynamic settling of a body. *J. Non-Newtonian Fluid Mech.* **183**, 25–36.
- 1027 MOROZOV, A. & SPAGNOLIE, S. E. 2015 Introduction to complex fluids. In *Complex Fluids in Biological* 1028 *Systems* (ed. S. E. Spagnolie), pp. 3–52. Springer.
- NIGEN, S. & WALTERS, K. 2002 Viscoelastic contraction flows: comparison of axisymmetric and planar configurations. *J. Non-Newtonian Fluid Mech.* **102** (2), 343–359.
- 1031 OBER, T. J., HAWARD, S. J., PIPE, C. J., SOULAGES, J. & McKINLEY, G. H. 2013 Microfluidic extensional rheometry using a hyperbolic contraction geometry. *Rheol. Acta* **52** (6), 529–546.
- 1033 Oldroyd, J. G. 1950 On the formulation of rheological equations of state. *Proc. R. Soc. A* **200** (1063), 1034 523–541.
- 1035 OWENS, R. G. & PHILLIPS, T. N. 2002 Computational rheology. Imperial College Press.
- 1036 Pearson, J. R. A. 1985 Mechanics of Polymer Processing. Elsevier.
- 1037 REMMELGAS, J., SINGH, P. & LEAL, L G. 1999 Computational studies of nonlinear elastic dumbbell models of Boger fluids in a cross-slot flow. *J. Non-Newtonian Fluid Mech.* **88** (1-2), 31–61.
- 1039 Renardy, M. 2000 Asymptotic structure of the stress field in flow past a cylinder at high Weissenberg number. *J. Non-Newtonian Fluid Mech.* **90** (1), 13–23.
- 1041 Ro, J. S. & Homsy, G. M. 1995 Viscoelastic free surface flows: thin film hydrodynamics of Hele-Shaw and dip coating flows. *J. Non-Newtonian Fluid Mech.* **57** (2-3), 203–225.
- ROTHSTEIN, J. P. & McKinley, G. H. 1999 Extensional flow of a polystyrene Boger fluid through a 4: 1: 4 axisymmetric contraction/expansion. *J. Non-Newtonian Fluid Mech.* **86** (1-2), 61–88.
- ROTHSTEIN, J. P. & McKinley, G. H. 2001 The axisymmetric contraction—expansion: the role of extensional rheology on vortex growth dynamics and the enhanced pressure drop. *J. Non-Newtonian Fluid Mech.* **98** (1), 33–63.
- SAPRYKIN, S., KOOPMANS, R. J. & KALLIADASIS, S. 2007 Free-surface thin-film flows over topography: influence of inertia and viscoelasticity. *J. Fluid Mech.* **578**, 271–293.
- SAWYER, W. G. & TICHY, J. A. 1998 Non-Newtonian lubrication with the second-order fluid. *J. Tribol.* 1051 120 (3), 622–628.

- Sousa, P. C., Coelho, P. M., Oliveira, M. S. N. & Alves, M. A. 2009 Three-dimensional flow of Newtonian and Boger fluids in square–square contractions. *J. Non-Newtonian Fluid Mech.* **160** (2-3), 122–139.
- 1054 STEINBERG, V. 2021 Elastic turbulence: an experimental view on inertialess random flow. *Annu. Rev. Fluid* 1055 *Mech.* **53**, 27–58.
- 1056 Su, Y., Castillo, A., Pak, O. S., Zhu, L. & Zenit, R. 2022 Viscoelastic levitation. J. Fluid Mech. 943, A23.
- 1057 SZABO, P., RALLISON, J. M. & HINCH, E. J. 1997 Start-up of flow of a FENE-fluid through a 4:1:4 constriction in a tube. *J. Non-Newtonian Fluid Mech.* **72** (1), 73–86.
- TICHY, J. A. 1996 Non-Newtonian lubrication with the convected Maxwell model. *Trans. ASME J. Tribol.* **118**, 344–348.
- Van Gorder, R. A., Vajravelu, K. & Akyildiz, F. T. 2009 Viscoelastic stresses in the stagnation flow of a dilute polymer solution. *J. Non-Newtonian Fluid Mech.* **161** (1-3), 94–100.
- VARCHANIS, S., TSAMOPOULOS, J., SHEN, A. Q. & HAWARD, S. J. 2022 Reduced and increased flow resistance in shear-dominated flows of Oldroyd-B fluids. *J. Non-Newtonian Fluid Mech.* **300**, 104698.
- Westein, E., van der Meer, A. D., Kuijpers, M. J. E., Frimat, J.-P., van den Berg, A. & Heemskerk, J.
 W. M. 2013 Atherosclerotic geometries exacerbate pathological thrombus formation poststenosis in a von Willebrand factor-dependent manner. *Proc. Natl. Acad. Sci. USA* 110 (4), 1357–1362.
- ZHANG, Y. L., MATAR, O. K. & CRASTER, R. V. 2002 Surfactant spreading on a thin weakly viscoelastic film. *J. Non-Newtonian Fluid Mech.* **105** (1), 53–78.
- ZOGRAFOS, K., HARTT, W., HAMERSKY, M., OLIVEIRA, M. S. N., ALVES, M. A. & POOLE, R. J. 2020
 Viscoelastic fluid flow simulations in the e-VROCTM geometry. J. Non-Newtonian Fluid Mech. 278, 104222.